Meso-scale turbulence in living fluids

Henricus H. Wensink[a,b], Jörn Dunkel[c,1], Sebastian Heidenreich[d], Knut Drescher[c,e], Raymond E. Goldstein[c], Hartmut Löwen[a], and Julia M. Yeomans[f]

[a]Institute for Theoretical Physics II: Soft Matter, Heinrich-Heine-Universität Düsseldorf, Universitätsstraße 1, D-40225 Düsseldorf, Germany; [b]Laboratoire de Physique des Solides, Université Paris-Sud 11, Bâtiment 510, 91405 Orsay Cedex, France; [c]DAMTP, Centre for Mathematical Sciences, University of Cambridge, Wilberforce Road, Cambridge CB3 0WA, United Kingdom; [d]Physikalisch-Technische Bundesanstalt, Abbestr. 2-12, 10587 Berlin, Germany; [e]Departments of Molecular Biology and Mechanical and Aerospace Engineering, Princeton University, Princeton, NJ 08544; and [f]Rudolf Peierls Centre for Theoretical Physics, University of Oxford, 1 Keble Road, Oxford OX1 3NP, United Kingdom

Edited by David A. Weitz, Harvard University, Cambridge, MA, and approved July 20, 2012 (received for review February 3, 2012)

Turbulence is ubiquitous, from oceanic currents to small-scale biological and quantum systems. Self-sustained turbulent motion in microbial suspensions presents an intriguing example of collective dynamical behavior among the simplest forms of life and is important for fluid mixing and molecular transport on the microscale. The mathematical characterization of turbulence phenomena in active nonequilibrium fluids proves even more difficult than for conventional liquids or gases. It is not known which features of turbulent phases in living matter are universal or system-specific or which generalizations of the Navier–Stokes equations are able to describe them adequately. Here, we combine experiments, particle simulations, and continuum theory to identify the statistical properties of self-sustained meso-scale turbulence in active systems. To study how dimensionality and boundary conditions affect collective bacterial dynamics, we measured energy spectra and structure functions in dense *Bacillus subtilis* suspensions in quasi-2D and 3D geometries. Our experimental results for the bacterial flow statistics agree well with predictions from a minimal model for self-propelled rods, suggesting that at high concentrations the collective motion of the bacteria is dominated by short-range interactions. To provide a basis for future theoretical studies, we propose a minimal continuum model for incompressible bacterial flow. A detailed numerical analysis of the 2D case shows that this theory can reproduce many of the experimentally observed features of self-sustained active turbulence.

low Reynolds number swimming | velocity increment distributions | scaling

Simple forms of life, like amoebae or bacteria, self-organize into remarkable macroscopic patterns (1, 2), ranging from extended networks (3, 4) to complex vortices (5–10) and swarms (11). These structures often bear a striking resemblance to assemblies of higher organisms [e.g., flocks of birds (12) or schools of fish (13, 14)] and present important biological model systems to study nonequilibrium phases and their transitions (15–17). A particularly interesting manifestation of collective behavior in microbial suspensions is the emergence of meso-scale turbulent motion (7, 8, 18, 19). Driven by the microorganisms' self-propulsion and their mutual interactions, such self-sustained "active turbulence" can have profound effects on nutrient mixing and molecular transport in microbiological systems (2, 20–22). However, in spite of recent progress (19, 23–25), the phenomenology of turbulent bacterial dynamics is scarcely understood and a commonly accepted theoretical description is lacking (2, 16, 26). The latter fact may not be surprising given that a comprehensive mathematical characterization of turbulence in conventional fluids has remained elusive after more than a century of intense research (27).

In view of the various physical and chemical pathways through which bacteria may communicate (1, 11, 28), a basic yet unsolved problem is to identify those interactions that are responsible for the emergence of collective behavior in dense suspensions (2, 29, 30). Answering this question is essential for understanding whether physical mechanisms such as flagellar bundling or hydrodynamic long-range interactions are relevant to collective bacterial motion; it is also crucial for constraining the vast number of theoretical models that have been proposed during the past two decades (2, 16, 19, 31, 32) but have yet to be tested against experiments. An equally important, unresolved issue pertains to the "universality" of turbulent phenomena in active systems and their relation to turbulence in passive fluids (27). In ordinary liquids and gases, such as water or air, turbulent vortices form due to external forcing if the Reynolds number (Re), the ratio of inertial to viscous forces, is very large ($\mathrm{Re} \gg 1$). By contrast, bacteria provide an internal microscopic forcing and operate at $\mathrm{Re} \sim 10^{-5}$ (33). It is therefore unclear how, or to what extent, the characteristics of self-sustained turbulent states in microbial suspensions differ from those of classical turbulence in passive fluids.

Here, we combine numerical simulations, high-speed microscopic imaging and continuum theory to identify generic statistical properties of active turbulent motion in dense bacterial systems, using *Bacillus subtilis* as a model organism. Unlike previous investigations of collective bacterial swimming in 2D free-standing films (8) and 3D bulk suspensions with liquid–gas interfaces (7, 24, 25), we conducted experiments in closed quasi-2D and 3D microfluidic chambers to minimize external influences and to compare the effects of boundary conditions and dimensionality. Our analysis focuses on traditional turbulence measures, such as energy spectra and velocity structure functions (27, 34, 35). These quantities have been widely studied for turbulent high-Re Navier-Stokes flow (27, 36–41), but their characteristics are largely unknown for active fluids. We compare our experimental results with large-scale simulations of a 2D minimal model for self-propelled rods. In the past, similar models (42) have proven useful for identifying generic aspects of flocking and swarming in active systems (43, 44). We find that, although the SPR model neglects details of bacterial cell–cell interactions, it is able to reproduce many features of our experimental data, suggesting that collective bacterial dynamics in dense suspensions is dominated by short-range interactions (30). We complement our experiments and particle-based simulation studies by identifying a minimal continuum model for incompressible active flow that combines elements from the Toner–Tu (15–17) and Swift–Hohenberg (45) theories.

Results

Motivation for the SPR Model. Self-motile bacteria may form meso-scale vortex patterns if their concentration is sufficiently large (7, 8, 18, 19). At very high volume fractions ($\phi \gtrsim 40\%$), steric repulsion and other short-range interactions (e.g., lubrication

Author contributions: H.H.W., J.D., S.H., K.D., R.E.G., H.L., and J.M.Y. designed research; H.H.W., J.D., S.H., and K.D. performed research; H.H.W., J.D., S.H., and K.D. contributed equally to the paper; H.H.W. and J.D. analyzed data; and H.H.W., J.D., S.H., K.D., R.E.G., H.L., and J.M.Y. wrote the paper.

The authors declare no conflict of interest.

This article is a PNAS Direct Submission.

Freely available online through the PNAS open access option.

[1]To whom correspondence should be addressed. E-mail: jd548@cam.ac.uk.

This article contains supporting information online at www.pnas.org/lookup/suppl/doi:10.1073/pnas.1202032109/-/DCSupplemental.

forces, flagellar bundling of neighboring cells) can be expected to govern physical reorientation and alignment, whereas intrinsic Brownian motion effects (30) become less important in this collision-dominated high-density regime (46). Chemotaxis (7, 18) can strongly affect bacterial dynamics in droplets or near liquid–gas interfaces but is less relevant in closed chambers as considered in our experiments. Recent direct measurements of individual *Escherichia coli* flow fields (30) suggest that hydrodynamic far-field interactions are negligible for bacterial reorientation, especially when bacteria swim close to a no-slip surface. Earlier experiments (8, 24, 25) on 2D films and 3D bulk suspensions also show that the average swimming speeds of individual bacteria [typically of the order of 10 μm/s in isolation (8, 30)] can be enhanced up to five times through collective hydrodynamic near-field effects. In the simplest approximation, however, a sufficiently dense bacterial suspension can be viewed as a system of deterministic, self-propelled, rod-like particles with an effective swimming speed V (for *B. subtilis* at $\phi \sim 40\%$ we find $V \sim 30$ to 100 μm/s depending on oxygen concentration and boundary conditions). One of our objectives is to test such a minimal model against experiments in the limit of highly concentrated suspensions and to provide systematic guidance for more accurate future models.

Non-Equilibrium Phase Diagram of the SPR Model. To identify generic requirements for the formation of turbulent phases in active systems, we performed simulations of a minimal 2D SPR model with periodic boundary conditions (see *SI Appendix* for details). In its simplest form, the model assumes that a rod-shaped self-propelled particle moves deterministically in the overdamped low-Re regime with an effective swimming speed V, while interacting with the other particles by steric forces. Mutual repulsion is implemented by discretizing each rod into spherical segments and imposing a repulsive Yukawa force potential $\sim \exp(-r/\lambda)/r$, where r is the distance, between the segments of any two rods (i.e., the decay length $\lambda > 0$ defines the effective diameter of a rod of length ℓ). If two sufficiently long rods perform a pair collision, this short-range interaction results in an effective nematic (apolar) alignment, before the rods become pushed apart by the repulsive force.

Depending on the effective volume filling fraction ϕ and the rod aspect ratio a, both defined in terms of the scale parameter λ and rod length ℓ, the SPR model exhibits a range of qualitatively different dynamical phases (Fig. 1). The numerically estimated nonequilibrium phase diagram (Fig. 1*A*) illustrates the importance of the effective particle "shape" in 2D: Upon increasing ϕ, short rods undergo a transition from a dilute state (D), with little or no cooperative motion, to a jammed state (J); this transition can be identified by the mean square displacement per particle, which drops off nearly two orders in magnitude along the transition curve. By contrast, very long rods ($a > 13$) do not jam at moderate filling fractions but exhibit swarming (S) behavior and large spatiotemporal density fluctuations. Generally, the transitions from the dilute phase (D) to cooperative motion (regions S, B and T) can be characterized by the Onsager overlap density (47). Upon increasing ϕ further, very long rods tend to assemble in homogeneous lanes (L), corresponding to quasi-smectic regions of local polar order; the swarming-to-laning transition is signaled by a discontinuous increase in the correlation length of the two-particle velocity correlation function. The swarming (S) and laning (L) phases adjoin a so-called active bionematic (18) phase (B), where vortices and extended jet-like structures coexist (28, 45); this phase is characterized by large fluctuations of the local vortex density. Most importantly for the present study, however, the SPR model predicts homogeneous turbulent states (T) at high filling fractions and intermediate aspect ratios $3 \lesssim a \lesssim 13$, a range that covers typical bacterial values (e.g., $2 \lesssim a \lesssim 4$ for *E. coli* and $2 \lesssim a \lesssim 10$ for *B. subtilis* (*SI Appendix*, Fig. S7). The transition between bionematic and turbulent phase is also signaled by the velocity distribution, correlation functions and density fluctuations (*SI Appendix*, Figs. S3 and S4).

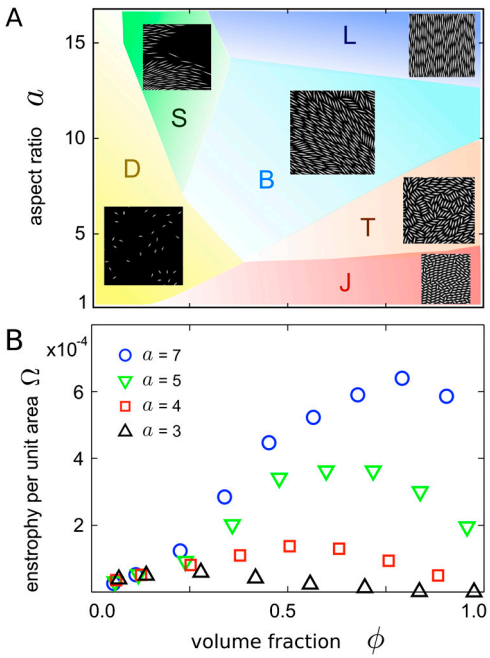

Fig. 1. (*A*) Schematic non-equilibrium phase diagram of the 2D SPR model and snapshots of six distinct phases from simulations: D-dilute state, J-jamming, S-swarming, B-bionematic phase, T-turbulence, L-laning (see also *SI Appendix*, Fig. S2 and Movies S1–S6). Our analysis focuses on the turbulent regime T. (*B*) Enstrophy per unit area Ω in units $(V/\lambda)^2$ for different aspect ratios $a = \ell/\lambda$, obtained from SPR simulations with $N \sim 10^4$ to 10^5 particles. The maxima of the enstrophy indicate the optimal filling fraction for active turbulence and mixing at a given value of the aspect ratio a. Note that values $\phi > 1$ are possible due to the softness of the repulsive force (see *SI Appendix* for simulation parameters).

Homogeneous Turbulent Phase in the SPR Model. A typical turbulent flow state as found in the simulations, and the associated (pseudo-scalar) 2D vorticity field $\omega = \partial_x v_y - \partial_y v_x$, are shown in Fig. 2. The mean local flow field $\boldsymbol{v}(t, \boldsymbol{r})$ at time t and position $\boldsymbol{r}$ was constructed by binning and averaging individual particle velocities, using a spatial resolution similar to that in our experiments (*SI Appendix*). To characterize the emergence of homogeneous turbulence in the SPR model in terms of particle geometry a and effective volume fraction ϕ, we quantify the vortical energy through the enstrophy (27, 34, 35) per unit area, $\Omega = \frac{1}{2}\overline{\langle|\omega(t,\boldsymbol{r})|^2\rangle}$, where brackets $\langle\cdot\rangle$ indicate spatial averages and overbars denote time averages. For slender rods ($a \geq 3$) the mean enstrophy Ω exhibits a maximum when plotted versus the volume fraction ϕ (Fig. 1*B*). This maximum coincides approximately with the transition from the bionematic to the turbulent phase; in a bacterial suspension, it corresponds to the optimal concentration for fluid mixing. Typical aspect ratios of bacterial cell bodies in our experiments lie in the range $2 \lesssim a \lesssim 10$ (mean 6.3 ± 1.2; see *SI Appendix*, Fig. S7). Hence, homogeneous bacterial turbulence should be observable in 2D for a broad range of filling fractions.

Experiments. We test the T-phase of the SPR model against experimental observations of *B. subtilis* at high filling fractions ($\phi \gtrsim 50\%$, see *Materials and Methods*). In contrast to recent investigations of bacterial dynamics in 2D free-standing films (8), on 2D surfaces (44, 48, 49) , and open 3D bulk suspensions (7, 18, 24, 25), bacteria were confined in closed microfluidic chambers to

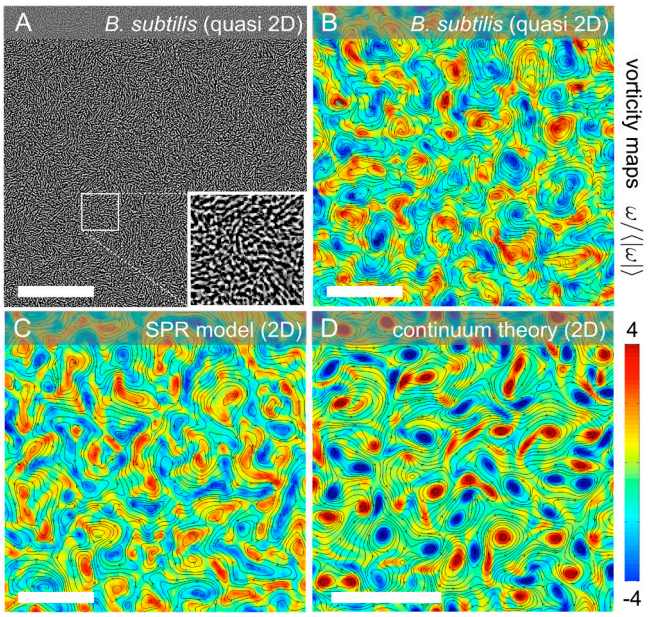

Fig. 2. Experimental snapshot (*A*) of a highly concentrated, homogeneous quasi-2D bacterial suspension (see also Movie S7 and *SI Appendix*, Fig. S8). Flow streamlines $\boldsymbol{v}(t, \boldsymbol{r})$ and vorticity fields $\omega(t, \boldsymbol{r})$ in the turbulent regime, as obtained from (*B*) quasi-2D bacteria experiments, (*C*) simulations of the deterministic SPR model ($a = 5$, $\phi = 0.84$), and (*D*) continuum theory. The range of the simulation data in *D* was adapted to the experimental field of view (217 μm × 217 μm) by matching the typical vortex size. (Scale bars, 50 μm.) Simulation parameters are summarized in *SI Appendix*.

minimize oxygen gradients that may cause anisotropic streaming of the oxytactic *B. subtilis* bacteria (2). To study the effects of dimensionality and boundary conditions, experiments were performed with two different setups: quasi-2D microfluidic chambers with a vertical height H less or equal to the individual body length of *B. subtilis* (approximately 5 μm) and 3D chambers with $H \approx 80$ μm (*SI Appendix*, Figs. S6 and S8 and Movies S7–S10). To focus on the collective dynamics of the microorganisms rather than the solvent flow (24, 50), we determined the mean local motion of *B. subtilis* directly using particle imaging velocimetry (PIV; see also *SI Appendix*). A typical snapshot from a quasi-2D experiment is shown in Fig. 2*A*. As evident from the inset, local density fluctuations that are important in the swarming/flocking regime (48, 49, 51) become suppressed at very high filling fractions (*SI Appendix*, Fig. S5). The corresponding flow fields (Fig. 2*B* and *SI Appendix*, Fig. S8) were used for the statistical analysis presented below.

Continuum Theory. The analytical understanding of turbulence phenomena hinges on the availability of simple yet sufficiently accurate continuum models (27). Considerable efforts have been made to construct effective field theories for active systems (15–17, 19, 31, 32, 52–54), but most of them have yet to be tested quantitatively against experiments. Many continuum models distinguish solvent velocity, bacterial velocity and/or orientational order parameter fields, resulting in a prohibitively large number of phenomenological parameters and making comparison with experiments very difficult. Aiming to identify a minimal hydrodynamic model of self-sustained meso-scale turbulence, we study a simplified continuum theory for incompressible active fluids, by focusing solely on the experimentally accessible velocity field $\boldsymbol{v}(t, \boldsymbol{r})$. By construction, the theory will not be applicable to regimes where density fluctuations are large (e.g., swarming or flocking), but it can provide a useful basis for quantitative comparisons with particle simulations and experiments at high concentrations.

We next summarize the model equations; a detailed motivation is given in *SI Appendix*. Because our experiments suggest that density fluctuations are negligible (Fig. 2*A*) we postulate incompressibility, $\nabla \cdot \boldsymbol{v} = 0$. The dynamics of $\boldsymbol{v}$ is governed by an incompressible Toner–Tu equation (15–17), supplemented with a Swift–Hohenberg-type fourth-order term (45),

$$(\partial_t + \lambda_0 \boldsymbol{v} \cdot \nabla)\boldsymbol{v} = -\nabla p + \lambda_1 \nabla \boldsymbol{v}^2 - (\alpha + \beta|\boldsymbol{v}|^2)\boldsymbol{v} + \Gamma_0 \nabla^2 \boldsymbol{v} - \Gamma_2 (\nabla^2)^2 \boldsymbol{v}, \qquad [1]$$

where p denotes pressure, and general hydrodynamic considerations (52) suggest that $\lambda_0 > 1$, $\lambda_1 > 0$ for pusher-swimmers like *B. subtilis* (see *SI Appendix*). The (α, β)-terms in Eq. **1** correspond to a quartic Landau-type velocity potential (15–17). For $\alpha > 0$ and $\beta > 0$, the fluid is damped to a globally disordered state with $\boldsymbol{v} = 0$, whereas for $\alpha < 0$ a global polar ordering is induced. However, such global polar ordering is not observed in suspensions of swimming bacteria, suggesting that other instability mechanisms prevail (53). A detailed stability analysis (*SI Appendix*) of Eq. **1** implies that the Swift–Hohenberg-type (Γ_0, Γ_2)-terms provide the simplest generic description of self-sustained meso-scale turbulence in incompressible active flow: For $\Gamma_0 < 0$ and $\Gamma_2 > 0$, the model exhibits a range of unstable modes, resulting in turbulent states as shown in Fig. 2*D*. Intuitively, the (Γ_0, Γ_2)-terms describe intermediate-range interactions, and their role in Fourier space is similar to that of the Landau potential in velocity space (*SI Appendix*). We therefore expect that Eq. **1** describes a wide class of quasi-incompressible active fluids. To compare the continuum model with experiments and SPR simulations, we next study traditional turbulence measures.

Velocity Structure Functions. Building on Kolmogorov's seminal work (55), a large part of the classical turbulence literature (27, 34, 36–38, 40, 41) focuses on identifying the distribution of the flow velocity increments $\delta\boldsymbol{v}(t, \boldsymbol{r}, \boldsymbol{R}) = \boldsymbol{v}(t, \boldsymbol{r} + \boldsymbol{R}) - \boldsymbol{v}(t, \boldsymbol{r})$. Their statistics is commonly characterized in terms of the longitudinal and transverse projections, $\delta v_\parallel = \hat{\boldsymbol{R}} \cdot \delta\boldsymbol{v}$ and $\delta v_\perp = \hat{\boldsymbol{T}} \cdot \delta\boldsymbol{v}$, where $\hat{\boldsymbol{T}} = (\epsilon_{ij}\hat{R}_j)$ denotes a unit vector perpendicular to the unit shift vector $\hat{\boldsymbol{R}} = \boldsymbol{R}/|\boldsymbol{R}|$. The separation-dependent statistical moments of $\delta v_\parallel$ and $\delta v_\perp$ define the longitudinal and transverse velocity structure functions

$$S^n_{\parallel,\perp}(\boldsymbol{R}) := \langle (\delta v_{\parallel,\perp})^n \rangle, \qquad n = 1, 2, \ldots. \qquad [2]$$

These functions have been intensely studied in turbulent high-Re fluids (27, 34, 35, 41) but are unknown for active flow. For isotropic steady-state turbulence, spatial averages $\langle \cdot \rangle$ as in Eq. **2** become time-independent, and the moments $S^n_{\parallel,\perp}$ reduce to functions of the distance $R = |\boldsymbol{R}|$.

Velocity distributions, increment distributions, and structure functions for our numerical and experimental data are summarized in Fig. 3. For the SPR model, the velocity statistics can be calculated either from the raw particle data or from pre-binned flow field data. The two methods produce similar results, and Fig. 3 shows averages based on individual particle velocities. Generally, we find that both the 2D SPR model and the 2D continuum simulations are capable of reproducing the experimentally measured quasi-2D flow histograms (Fig. 3 *A* and *B*) and structure functions (Fig. 3*C*). The maxima of the even transverse structure $S^{2n}_\perp$ signal a typical vortex size R_v, which is substantially larger in 3D bulk flow than in quasi-2D bacterial flow. Unlike their counterparts in high-Re Navier–Stokes flow (27, 34), the structure functions of active turbulence exhibit only a small region of power law growth for $\ell \lesssim R \ll R_v$ and flatten at larger distances (Fig. 3*C*).

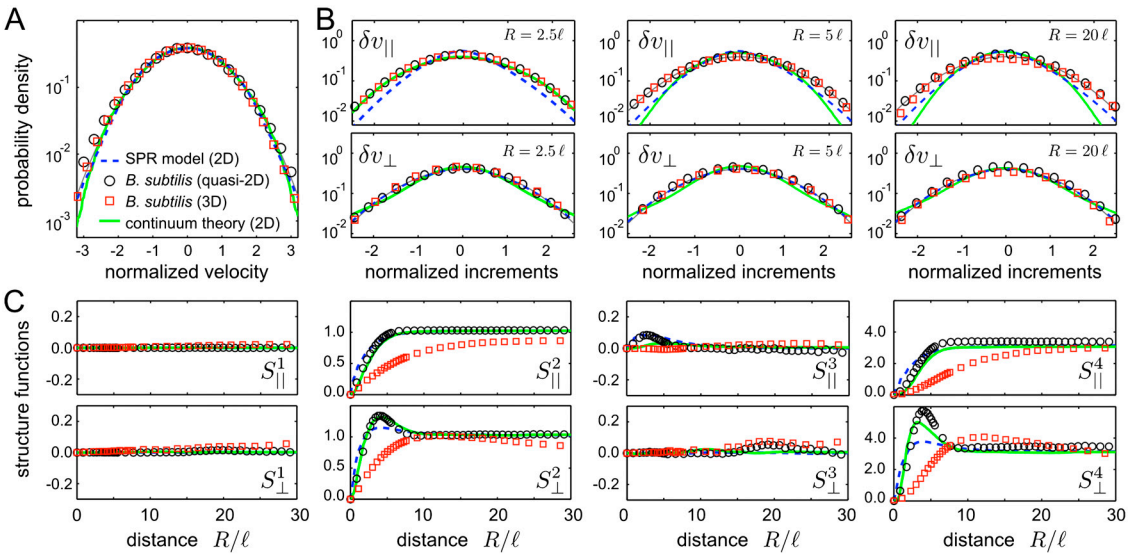

Fig. 3. Velocity statistics of self-sustained turbulent phases in active suspensions. (*A*) The marginal distributions of the normalized Cartesian velocity components $[v_i - \langle v_i \rangle]/[\langle v_i^2 \rangle - \langle v_i \rangle^2]^{1/2}_{i=x,y}$ are approximately Gaussian (thin gray line) for experiments, SPR model, and continuum theory. (*B*) The distributions of the longitudinal and transverse velocity increments $\delta v_{\parallel,\perp}$, normalized by their first and second moments $S^{1,2}_{\parallel,\perp}$ are shown for three different separations R. (*C*) Longitudinal and transverse velocity structure functions $S^n_{\parallel,\perp}$ normalized by $\langle v^2 \rangle^{n/2}$. The maxima of the even transverse structure functions $S^{2k}_{\perp}$ reflect the typical vortex size R_v , which is significantly larger in the 3D experiments. Experimental and theoretical data points are spatio-temporal averages over two orthogonal directions in *A* and *B* and all directions in *C*, yielding a typical sample size $>10^6$ per plotted data point in *C*. Histograms and structure functions for quasi-2D (3D) curves were obtained by combining PIV data from two (15) movies, respectively, representing an average over $2 \times 1{,}000$ (15×300) frames. Simulation parameters are identical to those in Fig. 2 and summarized in *SI Appendix*. Error bars are smaller than symbols.

Velocity Correlations and Flow Spectra. The energy spectrum $E(k)$, formally defined by $\langle \boldsymbol{v}^2 \rangle = 2\int_0^\infty E(k)dk$, reflects the accumulation of kinetic energy over different length scales. By virtue of the Wiener–Khinchine theorem (27), $E(k)$ can be estimated by Fourier transformation of the equal-time two-point velocity correlation function, yielding in d dimensions

$$E_d(k) = \frac{k^{d-1}}{C_d} \int d^d R \, \mathrm{e}^{-i\boldsymbol{k}.\boldsymbol{R}} \langle \boldsymbol{v}(t,\boldsymbol{r}) \cdot \boldsymbol{v}(t,\boldsymbol{r}+\boldsymbol{R}) \rangle, \qquad [3]$$

where $C_2 = 2\pi$ and $C_3 = 4\pi$. Normalized velocity correlation functions $\langle \boldsymbol{v}(t,\boldsymbol{r}) \cdot \boldsymbol{v}(t,\boldsymbol{r}+\boldsymbol{R}) \rangle$ and spectra $E_d(k)$ for our data are summarized in Fig. 4. The crossover from positive to negative correlations indicates again the typical vortex size R_v, in agreement with Fig. 3*C* and previous findings for open 3D bulk systems (7, 18).

In bacterial suspensions, the microorganisms inject kinetic energy on small scales $R \sim \ell$, setting the upper bound $k_\ell = 2\pi/\ell$ for the spectral range of the bacterial fluid. For both experiments and simulations, we observe turbulent vortices on scales $R > \ell$, which formally correspond to the energy-inertial range $k < k_\ell$ in classical 2D turbulence (34, 35). Our experimental and numerical data suggest asymptotic power law scaling regimes for small and large k-values (see Fig. 4*B*), but the power-law exponents differ from the characteristic $k^{-5/3}$-decay of 2D Kolmogorov–Kraichnan turbulence (39); see discussion below. The spectra for the 2D continuum model and the quasi-2D bacteria experiments are in good agreement, both showing large-k scaling with approximately $E(k) \sim k^{-8/3}$ and small-k scaling with roughly $E(k) \sim k^{+5/3}$. The asymptotic spectra for the 2D SPR model and the 3D experimental data look qualitatively similar but do also exhibit an intermediate plateau region, which indicates that kinetic energy is more evenly distributed over a range of scales.

Conclusions

SPR Model vs. Experiment. The deterministic SPR model provides a simplified description of the bacterial dynamics, because it neglects not only elastic properties of flagella and cell body but also hydrodynamic interactions and orientational fluctuations due to intrinsic swimming variability and thermal effects (30, 46). Notwithstanding, at high concentrations, such a minimal model reproduces remarkably well the flow velocity distributions and the structure functions from our quasi-2D *B. subtilis* experiments and the 2D continuum simulations (Fig. 3). This implies that hydrodynamic interactions per se are not required for the formation of self-sustained turbulence in dense suspensions—self-propulsion, a rod-like shape and volume exclusion interactions are sufficient (this raises the question whether the optimization of collective behavior may have been a factor in the evolution of bacterial shapes). However, to achieve a better quantitative agreement, particle-based future studies should focus on more realistic models that account for hydrodynamic near-field interactions and intrinsic randomness in bacterial swimming (30). The

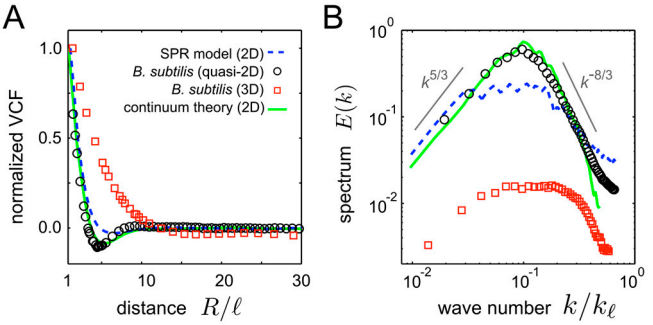

Fig. 4. Equal-time velocity correlation functions (VCFs), normalized to unity at $R = \ell$, and flow spectra for the 2D SPR model ($a = 5$, $\phi = 0.84$), *B. subtilis* experiments, and 2D continuum theory based on the same data as in Fig. 3. (*A*) The minima of the VCFs reflect the characteristic vortex size R_v (48). Data points present averages over all directions and time steps to maximize sample size. (*B*) For bulk turbulence (red squares) the 3D spectrum $E_3(k)$ is plotted ($k_\ell = 2\pi/\ell$), the other curves show 2D spectra $E_2(k)$. Spectra for the 2D continuum theory and quasi-2D experimental data are in good agreement; those of the 2D SPR model and the 3D bacterial data show similar asymptotic scaling but exhibit an intermediate plateau region (spectra multiplied by constants for better visibility and comparison).

experimental results presented above provide a benchmark for evaluating such microscopic models (56).

Continuum Model and "Universality". The good agreement of the structure functions, spatial and temporal flow correlations (see also *SI Appendix*, Fig. S9), and spectra from the 2D continuum theory with those from the quasi-2D experiments suggests that this theory could be a viable model for dense suspensions. Because the instability mechanism in the continuum theory arises from a generic small-wave number expansion in Fourier space (see *SI Appendix*) that is analogous to the Landau expansion in order-parameter space for second-order phase transitions, we expect that the model applies to a wide range of quasi-incompressible active fluids. This would imply that meso-scale turbulent structures in these systems share "universal" long-wave length characteristics. We note that the theory as formulated in Eq. **1** only accounts for leading terms up to fourth-order and, therefore, becomes inaccurate for large velocities and wave numbers (see tails in Figs. 3 *A* and *B* and 4*B*). Nevertheless, this continuum model appears to capture the main statistical and dynamical features of the experimental data. Important future challenges include the analytical prediction of active flow spectra from Eq. **1**, detailed numerical studies of 3D bacterial bulk flows and comparisons of our experimental and numerical data with $\boldsymbol{Q}$-tensor models and other multi-order parameter theories (2, 16, 19, 31, 32).

Dimensionality, Boundaries, and Hydrodynamic Interactions. The quasi-2D experiments allow us to compare with 2D simulations that come close to experimental system sizes. Freestanding thin films (8) and bacterial mono-layers on open surfaces (44, 49), which may be more prone to intrinsic instabilities and external fluctuations, provide an alternative but nonequivalent realization of a 2D bacterial fluid. The crucial difference between freestanding 2D films and our closed quasi-2D setup is that the presence of no-slip boundaries in our experiments suppresses hydrodynamic long-range interactions between bacteria due to cancellation effects from the hydrodynamic images: An isolated dipole-like swimmer [as *E. coli* (30) and, most likely, *B. subtilis*] creates a stroke-averaged far-field flow that decays as approximately $1/r^2$ with distance r in a 3D fluid. When the same swimmer moves parallel to a nearby solid surface in an otherwise semi-infinite fluid, the flow components parallel to the boundary decay faster approximately $1/r^4$ (30). If, however, the swimmer is closely confined between two parallel no-slip walls, as in our quasi-2D experiments with $H \sim 4$ μm, then the flow field becomes exponentially damped at distances $|r| \gg H$ (57). By contrast, in freestanding 2D films the flow field generated by an isolated microorganism has a much longer range approximately $1/r$ (22, 58), suggesting that hydrodynamic interactions could play a more important role for collective behavior in these systems (8). The fact that the typical vortex size in 3D is larger than in quasi-2D could indicate stronger short-to-intermediate-distance hydrodynamic coupling in 3D bulk flow; it would therefore be interesting to perform a similar analysis for thin-film data (8). Generally, however, we expect hydrodynamic far-field interactions to be less important for the dynamics in very dense suspensions due to mutual hydrodynamic screening (59) and the small magnitude of bacterial flows fields (30), but they could act as a destabilizing noise (54, 60).

Low-Re vs. High-Re Turbulence. Conventional high-Re turbulence arises from energy input on large scales (e.g., stirring or shearing). In 3D flow the injected energy is redistributed to smaller scales via an energy-inertial downward cascade with $E_3 \sim k^{-5/3}$ (27). In 2D films, due to the suppression of vortex stretching (34, 35), there can be both an energy-inertial upward cascade with $E_2 \sim k^{-5/3}$ and an enstrophy-transfer downward cascade with $E_2 \sim k^{-3}$ (39). Remarkably, viscoelastic polymer solutions can exhibit turbulent features (e.g., spectral power law scaling) at Reynolds numbers as low as 10^{-3}, facilitated by a slow nonlinear response to external shear due to long intrinsic relaxation times of the polymers (61, 62). Our simulations and experiments suggest asymptotic spectral power law decays toward the bacterial energy injection scale $k_\ell = 2\pi/\ell$ that resemble the energy-inertial regime of classical turbulence but, due to viscous damping by the low-Re solvent, extend over a smaller range of length scales (roughly up to 10ℓ). The latter fact is reminiscent of viscoelastic turbulence (61), although the underlying physical mechanisms are very different.

In conclusion, bacterial or, more generally, self-sustained active "turbulence," shares some qualitative characteristics with classical turbulence on small scales while differing on larger scales. Our detailed statistical analysis shows that, as with inertial turbulence, a complete quantitative understanding of turbulent behavior in active systems poses a challenging task. The combined experimental, theoretical, and numerical results presented here may provide both qualitative and quantitative guidance for future studies that aim at identifying the basic principles of dynamical self-organization in living fluids.

Materials and Methods

B. subtilis cells (wild type strain 168) were streaked from a −80 °C stock onto an LB medium plate containing 1.5% agar. The plates were incubated at 37 °C for 12 h. A single colony from the plates was used to inoculate an overnight culture in Terrific Broth (Sigma), which was then back-diluted 1:200 into 50 mL of fresh tryptone broth, and grown at 37 °C on a shaker to mid-log phase. The culture was then concentrated 400 × by centrifugation at 4,000 × *g* for 3 min, and the pellet was resuspended by gentle vortexing, to not shear off the flagella. The concentrated culture was loaded into a polydimethylsiloxane (PDMS) microfluidic device, which was then sealed to reduce background fluid motion. The microfluidic device consisted of cylindrical measurement chambers (radius 100 μm, height 4 μm for quasi-2D measurements, and radius 750 μm, height 80 μm for 3D measurements). The samples were imaged in bright field with a 40 × /NA 1.4 oil immersion objective on a Nikon TI-E microscope. Images were acquired at 40 fps in 2D (camera: Pike, Allied Vision Technologies), and 100 fps and 200 fps in 3D (camera: Phantom v9.1, Vision Research). Compared with measurements in quasi-2D chambers at the same frame rate, the vertical superposition of bacteria leads to a reduced image quality in 3D samples; we therefore recorded the flow in 3D suspensions at a higher frame rate. For the 3D measurements, we imaged at the bottom and in the middle of the chamber, while for the quasi-2D measurements, we imaged in the middle of the chamber. A detailed description of the theoretical models and numerical methods is given in *SI Appendix*. Raw data and additional experimental movies can be downloaded from http://damtp.cam.ac.uk/user/gold/datarequests.html.

ACKNOWLEDGMENTS. The authors are grateful to Gareth Alexander, Thomas Angelini, Igor Aronson, Markus Bär, Howard Berg, Colm Connaughton, Sujoy Ganguly, Siegfried Hess, Vasily Kantsler, John Lister, Peter Lu, Timothy Pedley, Adriana Pesci, and David Weitz for very helpful discussions. S.H. acknowledges financial support from the Deutsche Forschungsgemeinschaft (DFG), Grant HE5995/1-1. This work was also supported by DFG via SFB TR6 (section D3), Engineering and Physical Sciences Research Council, and European Research Council.

1. Copeland MF, Weibel DB (2009) Bacterial swarming: A model system for studying dynamic self-assembly. *Soft Matter* 5:1174–1187.
2. Koch DL, Subramanian G (2011) Collective hydrodynamics of swimming microorganisms: Living fluids. *Annu Rev Fluid Mech* 43:637–659.
3. Tero A, et al. (2010) Rules for biologically inspired adaptive network design. *Science* 327:439–442.
4. Xavier JB, Martinez-Garcia E, Foster KR (2009) Social evolution of spatial patterns in bacterial biofilms: When conflict drives disorder. *Am Nat* 174:1–12.
5. Kessler JO, Wojciechowski M (1997) *Collective Behavior and Dynamics of Swimming Bacteria* (Oxford University Press, Oxford, UK), pp 417–450.
6. Berg HC (1997) Motile behavior of bacteria. *Phys Today* 53:24–29.
7. Dombrowski C, Cisneros L, Chatkaew S, Goldstein RE, Kessler JO (2004) Self-concentration and large-scale coherence in bacterial dynamics. *Phys Rev Lett* 93:098103.
8. Sokolov A, Aranson IS, Kessler JO, Goldstein RE (2007) Concentration dependence of the collective dynamics of swimming bacteria. *Phys Rev Lett* 98:158102.
9. Riedel IH, Kruse K, Howard J (2005) A self-organized vortex array of hydrodynamically entrained sperm cells. *Science* 309:300–303.

10. Tuval I, et al. (2005) Bacterial swimming and oxygen transport near contact lines. *Proc Natl Acad Sci USA* 102:2277–2282.
11. Kearns DB (2010) A field guide to bacterial swarming motility. *Nat Rev Microbiol* 8:634–644.
12. Cavagna A, et al. (2009) Scale-free correlations in starling flocks. *Proc Natl Acad Sci USA* 107:11865–11870.
13. Katz Y, Ioannou CC, Tunstro K, Huepe C, Couzin ID (2011) Inferring the structure and dynamics of interactions in schooling fish. *Proc Natl Acad Sci USA* 108:18720–18725.
14. Sumpter DJT (2006) The principles of collective animal behaviour. *Philos Trans R Soc B* 261:5–22.
15. Toner J, Tu Y, Ramaswamy S (2005) Hydrodynamics and phases of flocks. *Ann Phys* 318:170–244.
16. Ramaswamy S (2010) The mechanics and statistics of active matter. *Annu Rev Condens Matter Phys* 1:323–345.
17. Toner J, Tu Y (1998) Flocks, herds, and schools: A quantitative theory of flocking. *Phys Rev E* 58:4828–4858.
18. Cisneros LH, Cortez R, Dombrowski C, Goldstein RE, Kessler JO (2007) Fluid dynamics of self-propelled micro-organisms, from individuals to concentrated populations. *Exp Fluids* 43:737–753.
19. Wolgemuth CW (2008) Collective swimming and the dynamics of bacterial turbulence. *Biophys J* 95:1564–1574.
20. Guasto JS, Rusconi R, Stocker R (2012) Fluid mechanics of planktonic microorganisms. *Annu Rev Fluid Mech* 44:373–400.
21. Zaid IM, Dunkel J, Yeomans JM (2011) Lévy fluctuations and mixing in dilute suspensions of algae and bacteria. *J R Soc Interface* 8:1314–1331.
22. Kurtuldu H, Guasto JS, Johnson KA, Gollub JP (2011) Enhancement of biomixing by swimming algal cells in two-dimensional films. *Proc Natl Acad Sci USA* 108:10391–10395.
23. Aranson IS, Sokolov A, Kessler JO, Goldstein RE (2007) Model for dynamical coherence in thin films of self-propelled microorganisms. *Phys Rev E* 75:040901.
24. Ishikawa T, et al. (2011) Energy transport in a concentrated suspension of bacteria. *Phys Rev Lett* 107:028102.
25. Cisneros LH, Kessler JO, Ganguly S, Goldstein RE (2011) Dynamics of swimming bacteria: Transition to directional order at high concentration. *Phys Rev E* 83:061907.
26. Czirók A, Vicsek T (2000) Collective behavior of interacting self-propelled particles. *Physica A* 281:17–29.
27. Frisch U (2004) *Turbulence* (Cambridge University Press, Cambridge, UK).
28. Waters CM, Bassler BL (2005) Quorum sensing: Cell-to-cell communication in bacteria. *Annu Rev Cell Dev Biol* 21:319–346.
29. Sokolov A, Aranson IS (2009) Reduction of viscosity in suspension of swimming bacteria. *Phys Rev Lett* 103:148101.
30. Drescher K, Dunkel J, Cisneros LH, Ganguly S, Goldstein RE (2011) Fluid dynamics and noise in bacterial cell-cell and cell-surface scattering. *Proc Natl Acad Sci USA* 108:10940–10945.
31. Baskaran A, Marchetti MC (2009) Statistical mechanics and hydrodynamics of bacterial suspensions. *Proc Natl Acad Sci USA* 106:15567–15572.
32. Baskaran A, Marchetti MC (2008) Hydrodynamics of self-propelled hard rods. *Phys Rev E* 77:011920.
33. Purcell EM (1977) Life at low Reynolds number. *Am J Phys* 45:3–11.
34. Kellay H, Goldburg WI (2002) Two-dimensional turbulence: A review of some recent experiments. *Rep Prog Phys* 65:845–894.
35. Danilov SD, Gurarie D (2000) Quasi-two-dimensional turbulence. *Usp Fiz Nauk* 170:921–968.
36. Gotoh T, Fukuyama D, Nakano T (2002) Velocity field statistics in homogeneous steady turbulence obtained using a high-resolution direct numerical simulation. *Phys Fluids* 14:1065–1081.
37. Noullez A, Wallace G, Lempert W, Miles RB, Frisch U (1997) Transverse velocity increments in turbulent flow using the RELIEF technique. *J Fluid Mech* 339:287–307.
38. Camussi R, Benzi R (1997) Hierarchy of transverse structure functions. *Phys Fluids* 9:257–259.
39. Kraichnan RH, Montogomery D (1980) Two-dimensional turbulence. *Rep Prog Phys* 43:547–619.
40. Lewis GS, Swinney HL (1999) Velocity structure functions, scaling, and transitions in high-Reynolds-number Couette-Taylor flow. *Phys Rev E* 59:5457–5467.
41. Anselmet F, Gagne Y, Hopfinger EJ, Antonia RA (1984) High-order velocity structure functions in turbulent shear flows. *J Fluid Mech* 140:63–89.
42. Ginelli F, Peruani F, Bär M, Chaté H (2010) Large-scale collective properties of self-propelled rods. *Phys Rev Lett* 104:184502.
43. Darnton NC, Turner L, Rojevsky S, Berg HC (2010) Dynamics of bacterial swarming. *Biophys J* 98:2082–2090.
44. Zhang HP, Be'er A, Florin E-L, Swinney HL (2010) Collective motion and density fluctuations in bacterial colonies. *Proc Natl Acad Sci USA* 107:13626–13630.
45. Swift J, Hohenberg PC (1977) Hydrodynamic fluctuations at the convective instability. *Phys Rev A* 15:319–328.
46. Munk T, Höfling F, Frey E, Franosch T (2009) Effective Perrin theory for the anisotropic diffusion of a strongly hindered rod. *Europhys Lett* 85:30003.
47. Onsager L (1949) The effects of shape on the interaction of colloidal particles. *Ann NY Acad Sci* 51:627–659.
48. Zhang HP, Be'er A, Smith RS, Florin E, Swinney HL (2009) Swarming dynamics in bacterial colonies. *Europhys Lett* 87:48011.
49. Chen X, Dong X, Be'er A, Swinney HL, Zhang HP (2012) Scale-invariant correlations in dynamic bacterial clusters. *Phys Rev Lett* 108:148101.
50. Dunkel J, Putz VB, Zaid IM, Yeomans JM (2010) Swimmer-tracer scattering at low Reynolds number. *Soft Matter* 6:4268–4276.
51. Narayan V, Ramaswamy S, Menon N (2007) Long-lived giant number fluctuations in a swarming granular nematic. *Science* 317:105–108.
52. Pedley TJ (2010) Collective behaviour of swimming micro-organisms. *Exp Mech* 50:1293–1301.
53. Ramaswamy S (2002) Hydrodynamic fluctuations and instabilities in ordered suspensions of self-propelled particles. *Phys Rev Lett* 89:058101.
54. Saintillan D, Shelley M (2008) Instabilities, pattern formation and mixing in active suspensions. *Phys Fluids* 20:123304.
55. Kolmogorov AN (1941) The local structure of turbulence in incompressible viscous fluid for very large Reynolds number. *Dokl Akad Nauk SSSR* 30:299–303.
56. Hernandez-Ortiz JP, Underhill PT, Graham MD (2009) Dynamics of confined suspensions of swimming particles. *J Phys Condens Matter* 21:204107.
57. Liron N, Mochon S (1976) Stokes flow for stokeslet betwen to parallel flat plates. *J Eng Math* 10:287–303.
58. Guasto JS, Johnson KA, Gollub JP (2010) Oscillatory flows induced by microorganisms swimming in two dimensions. *Phys Rev Lett* 105:168102.
59. Muthukumar M, Edwards SF (1983) Screening of hydrodynamic interaction in a solution of rodlike macromolecules. *Macromolecules* 16:1475–1478.
60. Ryan SD, Haines BM, Beryland L, Ziebert F, Aranson IS (2011) Viscosity of bacterial suspensions: Hydrodynamic interactions and self-induced noise. *Phys Rev E* 83:050904(R).
61. Groisman A, Steinberg V (2000) Elastic turbulence in a polymer solution. *Nature* 405:53–55.
62. Goddard C, Hess O, Hess S (2010) Low Reynolds number turbulence in nonlinear Maxwell-model fluids. *Phys Rev E* 81:036310.

Supporting Information Appendix: Meso-scale turbulence in living fluids

Henricus H. Wensink [*] [†], **Jörn Dunkel** [‡], **Sebastian Heidenreich** [§], **Knut Drescher** [‡] [¶], **Raymond E. Goldstein** [‡], **Hartmut Löwen** [*] **and Julia M. Yeomans** [‖]

[*]Institute for Theoretical Physics II: Soft Matter, Heinrich-Heine-Universität Düsseldorf, Universitätsstraße 1, D-40225, Düsseldorf, Germany, [†]Laboratoire de Physique des Solides, Université Paris-Sud 11, Bâtiment 510, 91405 Orsay Cedex, France, [‡]DAMTP, Centre for Mathematical Sciences, University of Cambridge, Wilberforce Road, Cambridge CB3 0WA, UK, [§]Physikalisch-Technische Bundesanstalt, Abbestr. 2-12, 10587 Berlin, Germany, [¶]Departments of Molecular Biology and Mechanical and Aerospace Engineering, Princeton University, Princeton, New Jersey 08544, USA, and [‖]Rudolf Peierls Centre for Theoretical Physics, University of Oxford, 1 Keble Road, Oxford OX1 3NP, UK

SPR Model

Dynamics. We simulate a system of N rigid rods of length ℓ, moving in a 2D volume A with periodic boundary conditions. Steric rod-rod interactions are represented by a segment model, i.e., each rod is partitioned into n equidistant segments. All segments from different rods interact with each other via a Yukawa potential [1]. The pair potential of two rods α and β, that have orientation unit vectors $\{\hat{\boldsymbol{u}}^\alpha, \hat{\boldsymbol{u}}^\beta\}$ and are separated by the center-of-mass distance $\Delta\boldsymbol{r}^{\alpha\beta}$, is given by

$$U^{\alpha\beta} = \frac{U_0}{n^2}\sum_{i=1}^{n}\sum_{j=1}^{n}\frac{\exp(-r_{ij}^{\alpha\beta}/\lambda)}{r_{ij}^{\alpha\beta}}. \qquad [1]$$

Here, U_0 is the potential amplitude, λ the screening length, and

$$r_{ij}^{\alpha\beta} = |\Delta\boldsymbol{r}^{\alpha\beta} + (l_i\hat{\boldsymbol{u}}^\alpha - l_j\hat{\boldsymbol{u}}^\beta)| \qquad [2]$$

the distance between the ith segment of rod α and the jth segment of rod β, with $l_i \in [-(\ell-\lambda)/2, (\ell-\lambda)/2]$ denoting the position of segment i along the symmetry axis of the rod α. The screening length λ defines the effective diameter of the segments. The 'shape' of a rod of length ℓ is then determined by the aspect ratio

$$a = \ell/\lambda. \qquad [3]$$

The case $a = 1$ corresponds to a single Yukawa point particle ($n = 1$). For $a > 1$, the number of segments per rod is fixed as $n = 3$ for $1 < a \leq 3$ and $n = \lfloor 9a/8 \rceil$ for $a > 3$ with $\lfloor\cdot\rceil$ denoting the nearest integer.

Considering the dynamical regime relevant to microorganisms, we assume that the motion of the SPRs is overdamped due to solvent friction (zero Reynolds number limit Re = 0).

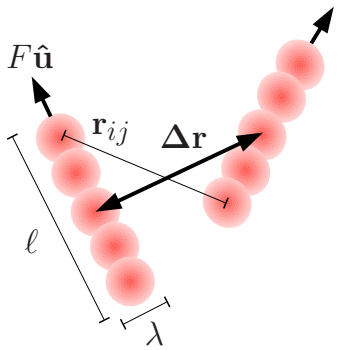

Fig. S1. Sketch of the SPR model. Each rod is represented by $n = 5$ repulsive Yukawa segments and has an aspect ratio $a = \ell/\lambda$. Self-propulsion is provided by a constant force F acting along the main rod axis indicated by the orientational unit vector $\hat{\boldsymbol{u}}$. The total rod pair potential is obtained by a sum over all Yukawa segment pairs with distance $\boldsymbol{r}_{ij}$ according to Eq. [1].

Since we are interested in the collision-dominated dynamics in dense bacterial suspensions, we neglect thermal and intrinsic [2] fluctuations of the bacterial orientation and restrict our study to deterministic motions. With these simplifying assumptions, the equations of motion for the center-of-mass $\boldsymbol{r}_\alpha(t)$ and orientation $\hat{\boldsymbol{u}}_\alpha(t)$ of an SPR are of first order in time and can be written in the compact form

$$\boldsymbol{f}_T \cdot \frac{d}{dt}\boldsymbol{r}_\alpha = F\hat{\boldsymbol{u}}_\alpha - \nabla_{\boldsymbol{r}_\alpha}U, \qquad [4]$$

$$\boldsymbol{f}_R \cdot \frac{d}{dt}\hat{\boldsymbol{u}}_\alpha = -\nabla_{\hat{\boldsymbol{u}}_\alpha}U. \qquad [5]$$

Here, F is a constant self-motility force acting along the longitudinal axis of each rod, $U = (1/2)\sum_{\beta,\alpha:\beta\neq\alpha}U^{\alpha\beta}$ the total potential energy, $\nabla_{\hat{\boldsymbol{u}}}$ denotes the gradient on the unit circle, and

$$\boldsymbol{f}_T = f_0\left[f_\parallel\hat{\boldsymbol{u}}\hat{\boldsymbol{u}} + f_\perp(\boldsymbol{I} - \hat{\boldsymbol{u}}\hat{\boldsymbol{u}})\right], \qquad [6]$$

$$\boldsymbol{f}_R = f_0 f_R\boldsymbol{I} \qquad [7]$$

are the translational and rotational friction tensors ($\boldsymbol{I}$ is the 2D unit tensor) with a Stokesian friction coefficent f_0. The dimensionless geometric factors $\{f_\parallel, f_\perp, f_R\}$ depend solely on the aspect ratio a, and we adopt the standard expressions for rod-like macromolecules, as given in Ref. [3]

$$\frac{2\pi}{f_{||}} = \ln a - 0.207 + \frac{0.980}{a} - \frac{0.133}{a^2}, \qquad [8]$$

$$\frac{4\pi}{f_{||}} = \ln a + 0.839 + \frac{0.185}{a} + \frac{0.233}{a^2}, \qquad [9]$$

$$\frac{\pi a^2}{3f_R} = \ln a - 0.662 + \frac{0.917}{a} - \frac{0.050}{a^2}. \qquad [10]$$

We note that after multiplication with the inverse matrix $\boldsymbol{f}_T^{-1}$, Eq. [4] can be rewritten as

$$\frac{d}{dt}\boldsymbol{r}_\alpha = V\hat{\boldsymbol{u}}_\alpha - \boldsymbol{f}_T^{-1}\cdot\nabla_{\boldsymbol{r}_\alpha}U, \qquad [11]$$

where

$$V = \frac{F}{f_0 f_{||}} \qquad [12]$$

defines the self-swimming speed of a non-interacting SPR. When comparing with dense bacterial suspensions, however, V should be interpreted as an effective parameter that is of the order of the mean self-swimming speed of a bacterium in suspension.

Simulations. In our simulations, we adopted characteristic units such that $\lambda = 1$, $F = 1$, and $f_0 = 1$, which means that distance is measured in units of λ, velocity in units of F/f_0, time in units of $\lambda f_0/F$ and energy in units of $F\lambda$. After rescaling to dimensionless coordinates, three relevant system parameters remain: The dimensionless Yukawa amplitude $\tilde{U}_0 = U_0/(F\lambda)$, which determines the hardness of the rod interactions relative to their characteristic propulsion energy,

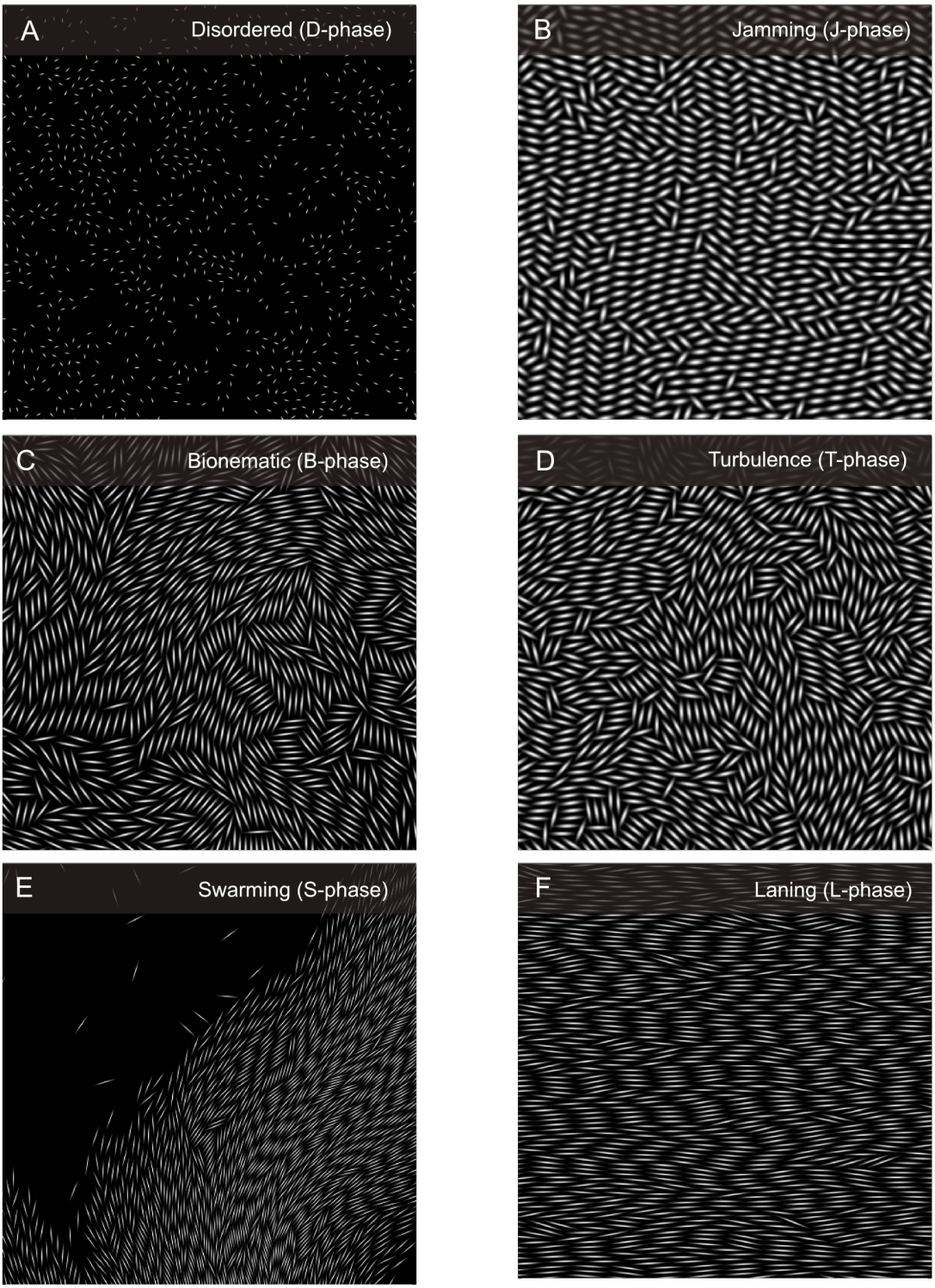

Fig. S2. Snapshots of the different phases of the SPR-model (see also Fig. 1A of the Main Text and Movies S1-S6). Each snapshot shows only a subsection of the full simulation volume, scaled to contain approximately the same mean particle number. Rod-shapes were fitted by elongated Gaussian intensity profiles. Generally, monodisperse SPR phases may exhibit regions of local smectic order (see E,F) that are absent in polydisperse bacterial suspensions. Simulation parameters: (A) particle number $N = 10,000$, aspect ratio $a = 4$, volume fraction $\phi = 0.063$, Yukawa amplitude $U_0 = 250$; (B) $N = 9996$, $a = 3$, $\phi = 0.975$, $U_0 = 250$; (C) $N = 9964$, $a = 9$, $\phi = 0.55$, $U_0 = 250$; (D) $N = 9968$, $a = 5$, $\phi = 0.84$, $U_0 = 250$; (E) $N = 9990$, $a = 16$, $\phi = 0.21$, $U_0 = 250$; (F) $N = 9996$, $a = 16$, $\phi = 0.53$, $U_0 = 250$.

the aspect ratio a, and the effective volume fraction of the system

$$\phi = \frac{N}{A}\left[\lambda(\ell-\lambda)+\frac{\pi\lambda^2}{4}\right], \qquad [13]$$

where A is the simulation volume. For sufficiently hard rods, the general dynamical behavior is only weakly dependent on the Yukawa amplitude, and we performed simulations for $\tilde{U}_0 = 250, 455, 500, 555, 625, 1250$. This leaves us with the rod shape a and volume fraction ϕ as the primary parameters. We simulated the evolution of the many-body SPR model as a function of time $\tau = tF/\lambda f_0$ in a square box of length L with periodic boundary conditions at volume fractions in the range $0.05 < \phi < 0.9$. Numerical studies were carried out using a time discretization $\Delta\tau = 0.002\rho^{-1/2}$, where $\rho = N\lambda^2/A$ with typically $N = 10^4 \div 10^5$ rods per simulation. Initial configurations, generated from a rectangular lattice of aligned rods with $\hat{\boldsymbol{u}}$ pointing randomly up or down were allowed to relax during an interval $\tau = 1000$ before statistics is gathered over an interval $\tau = 20L$ with $L = (N/\rho)^{1/2}$ the dimension of the simulation box (in units of λ). Velocity vector fields $\boldsymbol{v}(t,\boldsymbol{r})$ were constructed by measuring the average centre-of-mass velocity within small sub-cells centered around the position $\boldsymbol{r}$, as described below.

In order to test for finite size effects, we simulated two different system sizes: 'small' systems with $N = 1\cdot 10^4$ particles and 'large' systems with $N = 4\cdot 10^4$ particles at the same filling fraction ϕ. Generally, we found that statistical quantifiers are robust with respect to changes in the particle number N, provided N is at least of $\mathcal{O}(10^4)$.

Analysis of Simulation Data. The microscopic velocities of the SPRs follow directly from the equations of motion [**4**] and [**5**]. From the particle velocities we construct effective flow fields by projecting the particle positions onto a 2D cubic grid $\{(i,j) \mid 1 \le i,j \le G\}$ and measuring the average velocity $\boldsymbol{U}(t;i,j)$ in each bin (i,j) at a given time t. 2D vorticity maps for the SPR model, as shown Fig. 1B and Fig. 2A of the Main Text, were computed from such averaged flow field data. To increase the spatial resolution of the flow field, we allowed neighboring bins to have a 75% overlap (the same overlap was used in the PIV analysis of experimental data, see below). For instance, for a large system $N = 4\cdot 10^4$ particles and a total box length $L \sim 80\ell$, we used a bin width of $\delta = 1.31\ell$ so that each sub-cell contains approximately 10 rods. In this case, the resulting cubic grid consists of $G \times G = 97 \times 97$ overlapping cells. We verified that the statistical properties of the flow fields remained robust under moderate variations of the bin size. We generally found that results are stable if the bin size is moderately larger than the SPR length $\delta \gtrsim \ell$. However, if the bin size is chosen too large, $\delta \gg \ell$, structural information about vortices is lost.

For the SPR model, statistical quantifiers can be constructed either from the raw particle data or from pre-averaged effective flow fields. Both methods produce qualitatively similar results for the velocity statistics but quantitative differences of several percent are noticable. Figures 3 and 4 in the Main Text show results that were obtained by direct averaging of individual SPR velocities. The schematic phase diagram and the enstrophy curves in Fig. 1 of the Main Text, and the snapshots in Fig. S2 were computed using a Yukawa amplitude $U_0 = 250$. The SPR results (velocity histograms, structure functions, spectra, etc.) in Figs 2A, 3 and 4 of the Main Text are based on parameters $U_0 = 455$, $a = 5$, $\phi = 0.84$, as these values yield good quantitative agreement with the 2D experimental data.

Number Fluctuations. Additional information about the different dynamical phases of the SPR model can be obtained from the number fluctuations $\Delta N^2 = \langle (N_L - \langle N_L\rangle)^2\rangle$ of the average number of SPRs $\langle N_L\rangle = NL^2/A$ in a square subcompartment of linear size L (see Fig S3). From the power-law behaviour $\Delta N \propto \langle N_L\rangle^\gamma$ one can extract an exponent $\gamma = 0.9 \pm 0.2$ which reveal giant fluctuations in the swarming S-phase and bionematic B-phase (note that $\gamma = 0.5$ for a system in thermal equilibrium). The number fluctuations are much weaker for the dilute D-phase although the anomalous exponent ($\gamma \sim 0.6$) hints at some degree of clustering occuring even at low particle density, see also snapshots in Fig. S2. The crossover from S-swarming to T-turbulence in the phase diagram (see Fig. 1A of the Main Text) can be inferred from a steep decrease in the density fluctuations at lower packing fractions. The crossover represents a transition from strongly fluctuating flocking-type flow to homogeneous vortical flow where density fluctuations are suppressed due to packing effects. In particular, the marginal exponent ($\gamma = 0.3$) for the turbulent T-phase supports the assumption of incompressible flow in the continuum theory (see Main Text).

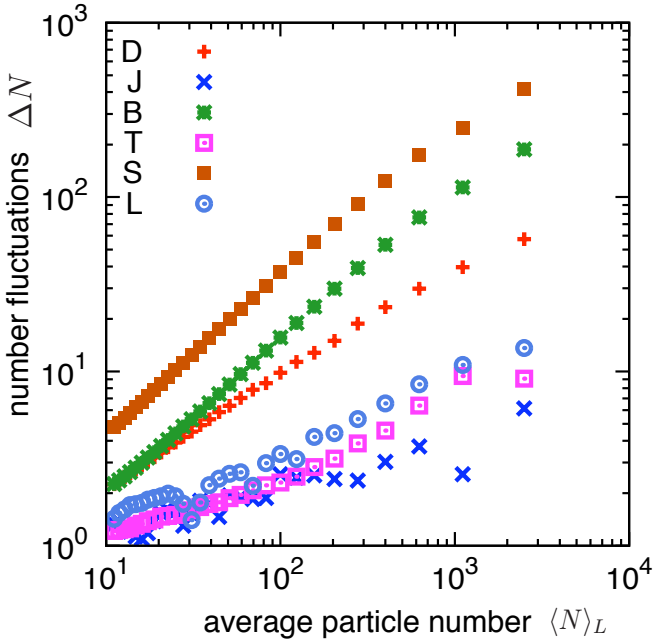

Fig. S3. Typical number fluctuations $\Delta N^2 = \langle (N_L - \langle N_L\rangle)^2\rangle$ as a function of the average particle number $\langle N_L\rangle$ (see text) for the different emergent states in a system of $N = 10^4$ SPR. The power-law scaling $\Delta N \propto \langle N_L\rangle^\gamma$ reveals giant number fluctuations ($\gamma \sim 1$) for the S-swarming ($a = 16, \phi = 0.21$) and B-bionematic ($a = 9, \phi = 0.55$) phases, while fluctuations are strongly suppressed ($\gamma < 0.5$) in the dense J-jamming ($a = 3$, $\phi = 0.97$), T-turbulence ($a = 5$, $\phi = 0.84$) and L-laning ($a = 16, \phi = 0.53$) phases, see also snapshots in Fig. S2. Note that $\gamma = 0.5$ for a system in thermal equilibrium.

Distinction between Turbulent and Bionematic Flow. The defining feature of the 'zooming' bionematic phase [4, 5] (here referred to as B-phase) is the existence of jet-like nematic regions, which determine the velocity statistics of the active flow (see Supplementary Movie S3 and also Fig. S2C). At high filling fractions, these jets become suppressed and the system crosses over into a homogeneous turbulent phase (T-phase), as illustrated in the schematic phase diagram (Fig. 1A) of the Main Text.

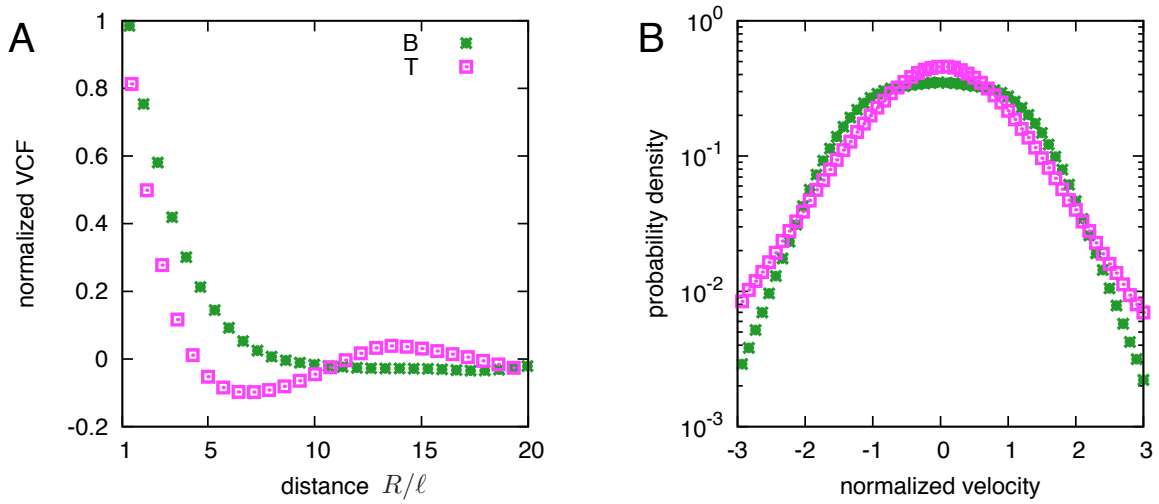

Fig. S4. Comparison of the bionematic B-phase and the turbulent T-phase of the SPR model. (A) Equal-time velocity correlation functions (VCFs), normalised to unity at $R = \ell$, and (B) distribution of the Cartesian velocity components for the B-phase ($a = 9$,$\phi = 0.55$) and T-turbulence ($a = 5$, $\phi = 0.84$). The turbulent T-phase exhibits negative velocity correlations that indicate a characteristic vortex size, and the velocity distribution is approximately Gaussian in the central regions with exponential tails. In contrast, the B-phase is characterized by a broadened non-Gaussian shape of the velocity distribution and a flattened VCF.

Statistical quantifiers that can be used to distinguish the B-phase from the T-phase are the velocity correlation function (VCF) and the marginal distribution of the SPR velocities. For the turbulent T-phase, the VCF of shows a clear minimum representing the typical vortex size and the velocity distribution becomes Gaussian in the central regions (see Fig. S4). By contrast, the B-phase is characterized by a strongly non-Gaussian (broadened) shape of the velocity distribution and the oscillations of the VCF are washed out due to existence of bionematic jets (see detailed discussion by Zhang et al. [6]). Furthermore, number fluctuations are much stronger in the B-phase than in the T-phase, as evident from Fig. S3.

Expected Validity and Limitations of the SPR Model. To assess the validity and limitations of the SPR model, it is useful to compare the phases in Fig. S2 with experimental observations reported in the literature [4, 5, 7, 6, 8] and results from our measurements. Representative snapshots of different phases, as observed in our quasi-2D experiments at different bacterial filling fractions, are shown in Fig. S5, see also Supplementary Movies S8-S10.

The dilute D-phase (Fig. S2A and Fig. S5A) was realized in the experiments of Sokolov et al. [7], who also observed the B-phase (Fig. S2C) in *B. subtilis* suspension confined to 2D thin films. The B-phase was also analyzed in detail by Cisneros et al. [4, 5] for *B. subtilis* in 3D open droplets and by Zhang et al. [6] for quasi-2D *Paenibacillus dendritiformis* colonies growing on agar. The correlation functions reported by these authors resemble closely those for the B-phase in the SPR model (Fig. S4). Swarming and flocking states of bacteria, similar to those in Fig. S2E and Fig. S5B, were studied by Zhang et al. [9] and Chen et al. [8] for *B. subtilis* grown on agar. To our knowledge, the jamming phase (Fig. S2B), which corresponds to a 'frozen' active crystal, and the laning phase (Fig. S2F) have not yet been realized in experiments with motile bacteria, although recent work by Volfson et al. [10] suggests that it could be possible to observe these phases for sufficiently long bacteria in suitably designed microfluidic chambers.

Generally, we would like to emphasize that, due to their simplicity, SPR models are not likely to capture quantitatively all the details of the bacterial dynamics in semi-dilute suspensions, where collective hydrodynamic effects and intrinsic ori-

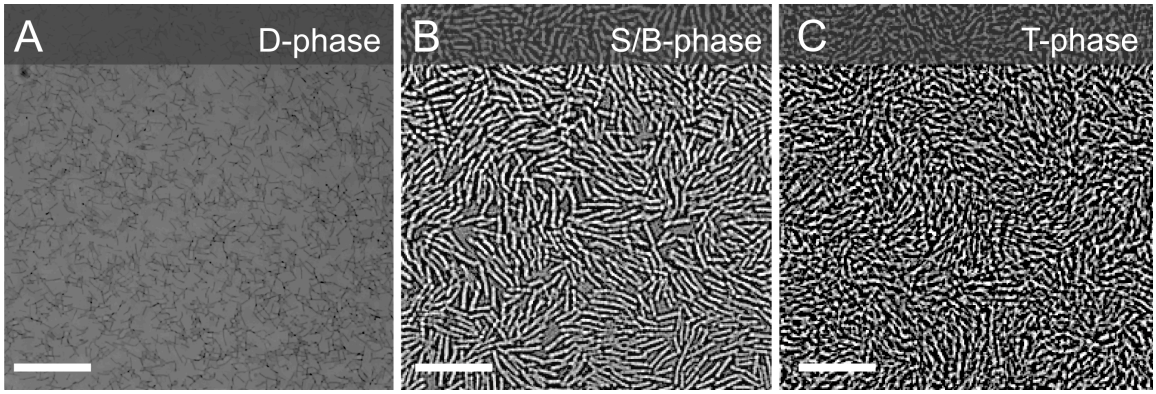

Fig. S5. Micrographs of quasi-2D *B. subtilis* suspensions in the (A) dilute phase at very low filling fractions, (B) near the swarming-bionematic transition at intermediate filling fractions, and (C) in the turbulent regime at very high filling fraction. Scale bars: (A) 30μm, (B,C) 10μm. Note the similarities with the corresponding SPR phases in Fig. S2, although some differences exist due to the varying SPR aspect ratios, the polydispersity of bacteria and the fact that the simulations are strictly 2D whereas the microfluidic chamber is only quasi-2D.

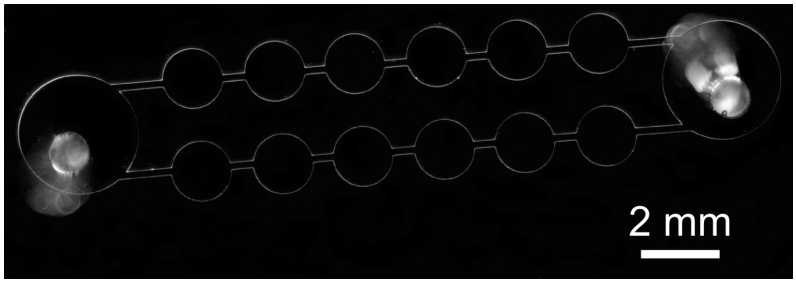

Fig. S6. Dark-field image (top view) of microfluidic chambers as used in the 3D experiments (channel height $80\,\mu$m, see also Materials and Methods). Bright spots in the two outer larger chambers are the inlets. Flow field measurements were performed in the small chambers. For the quasi-2D experiments, the same chamber geometry was used but with a reduced channel height of $5\,\mu$m.

entational noise in bacterial locomotion [2] become relevant. Deterministic SPR models can be expected to become more accurate the higher the bacterial concentration. This hypothesis appears to be supported by the good agreement for the velocity statistics from our quasi-2D experimental data and 2D SPR data for the T-phase (see Fig. 3 in the Main Text). However, even in the high-density regime, minor quantitative differences between our bacteria experiments and 2D simulations of monodisperse SPR systems are to be expected since (i) our chambers are only approximately 2D and (ii) bacterial suspensions are polydisperse (Fig. S7).

Analysis of Experimental Data

Imaging Parameters. Figure S6 shows microfluidic chambers as used in our experiments (see also Materials and Methods in the Main Text). Microscope images of dense *B. subtilis* suspensions (volume fractions $\phi \sim 0.4$) were recorded at frame rate f, corresponding to a time interval $\Delta t = t_k - t_{k-1} = 1/f$ between subsequent frames $k = 1, \ldots, K$. For the quasi-2D experiments we used an image resolution of 700 pix $\times$ 700 pix with conversion rate 0.31 μm/pix and frame rate $f = 40$ Hz, and for the 3D experiments 768 pix $\times$ 768 pix with 0.29 μm/pix and $f = 100$ Hz or $f = 200$ Hz.

Estimation of Bacterial Aspect Ratios. The aspect ratios of *B. subtilis* bacteria were determined directly from our imaging data, by analyzing a representative sample (randomly selected 2D layer) of bacteria from a diluted suspension (Fig. S7A). Bacterial shapes were fitted by capped cylinders (Fig. S7B) and the pixel counts were used to determine the histogram shown Fig. S7C, yielding a mean aspect ratio 6.3 ± 1.2.

Particle Imaging Velocimetry (PIV). To extract the local flow field components from the experimental movie data, we used the commercial PIV software Dantec Flow Manager. The PIV algorithm estimates the 2D velocity field $\boldsymbol{U}_P(t_k; i, j)$ at time t_k on a 2D cubic grid. In our analysis, we used averaging windows of size 32 pix $\times$ 32 pix, which roughly corresponds to $2\ell \times 2\ell$ in terms of the mean bacterial length $\ell \sim 4.8\,\mu$m for *B. subtilis* and is sufficiently large to contain ~ 10 bacteria but still small enough to resolve spatial flow field structures on the order of a few bacterial lengths. The distance between neighboring grid points was chosen to generate a 75% overlap between neighbouring bins. This corresponds to the highest spatial resolution that is achievable within this software for the given window size, resulting in a grid of size $G \times G = 84 \times 84$ for the quasi-2D data, and $G \times G = 93 \times 93$ for the 3D data. A comparison between PIV flow data for quasi-2D and 3D bacterial suspensions is shown in Fig. S8. One readily observes that the typical vortex size is considerably smaller in 2D than in 3D, see also Fig. 4A in the Main Text.

Correction of Systematic Errors. Flow field reconstruction via PIV can introduce systematic errors due to pixel locking (PL) [5]. We correct our flow field data $\boldsymbol{U}_P(t_k; i, j)$ obtained from the PIV algorithm for PL errors by using a calibration procedure similar to the one that is described in detail in the Appendix of Ref. [5]. The only minor modification adopted here is that, instead of generating a look-up table, we fitted the periodic residual errors by using trigonometric functions which were then used to reconstruct the corrected flow field $\boldsymbol{U}$ from $\boldsymbol{U}_P$. Furthermore, we also corrected $\boldsymbol{U}$ for small systematic drift effects (e.g., due to weak oxygen gradients caused by the inlets of the microfluidic chambers), by subtracting the

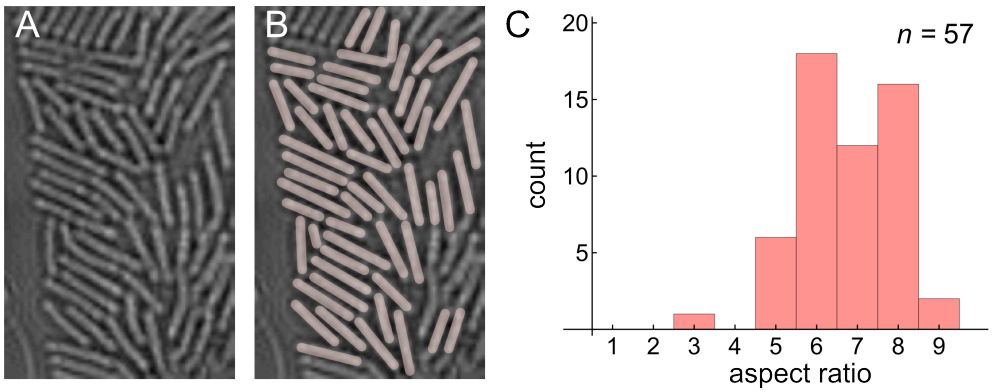

Fig. S7. Estimation of bacterial aspect ratios. (A) Micrograph showing a randomly selected 2D layer from a diluted *B. subtilis* suspension. (B) Bacterial shapes were manually fitted by capped cylinders (pink) and pixel counts were used to obtain the histogram in (C); mean value 6.3 ± 1.2.

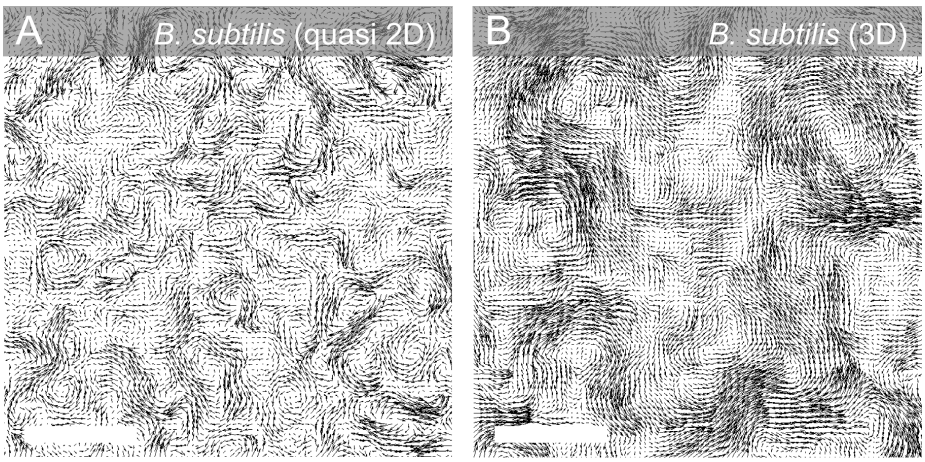

Fig. S8. Snapshots of PIV flow data for dense (A) quasi-2D and (B) 3D *B. subtilis* suspensions. Scale bars 50 μm. Arrow sizes in both diagrams are normalized to the same unit velocity; the maximum velocity in (A) is 26μm/s. The typical vortex size is considerably smaller in 2D than in 3D, see also Fig. 4A in the Main Text.

mean flow velocity

$$\overline{\langle \boldsymbol{U} \rangle} = \frac{1}{K} \sum_{t_k} \langle \boldsymbol{U}(t_k) \rangle = \frac{1}{K} \sum_{t_k} \frac{1}{G^2} \sum_{i,j} \boldsymbol{U}(t_k; i, j) \qquad [14]$$

from the calibrated data $\boldsymbol{U}(t_k; i, j)$, yielding the corrected data

$$\boldsymbol{u}(t_k; i, j) = \boldsymbol{U}(t_k; i, j) - \overline{\langle \boldsymbol{U} \rangle} \qquad [15]$$

used in our statistical analysis. The subtraction of the constant $\overline{\langle \boldsymbol{U} \rangle}$ does not affect the statistics of velocity increments, but modifies the values obtained for the total kinetic energy or the energy spectrum. Generally, we found that, while the shape of the velocity histograms can be strongly affected by PL effects, the velocity structure functions are not very sensitive ($< 1\%$) to the PL correction.

Continuum Model

We discuss the basic considerations that lead to the continuum model defined by Eq. [1] of the Main Text. This model aims to provide a phenomenological description of quasi-incompressible active fluids by combining elements from the Toner-Tu theory [11, 12] and the Swift-Hohenberg theory [13]. After summarizing the underlying ideas, we will present a linear stability analysis for the 2D case and conclude by commenting on the numerical implementation and parameter choices in our 2D simulations.

Basic Assumptions. Our main objective is to identify a minimal continuum theory that exhibits self-sustained dynamical vortex structures similar to those observed in the SPR simulations and in the *B. subtilis* experiments. To this end, we focus on the limit of very high bacterial concentrations (filling fractions). The model is based on two main assumptions that are guided by insights from the experiments and particle simulations:

1. At sufficiently high concentrations, the bacterial (or SPR) suspension becomes, in good approximation, an incompressible active fluid.
2. The essential dynamics of the bacterial fluid can be captured by a single vectorial order parameter field, the mean flow velocity $\boldsymbol{v}(t, \boldsymbol{x})$.

The incompressibility assumption appears to be justified by the fact that density fluctuations are very small in both our experiments and SPR simulations ($< 5\%$), provided the particle density is sufficiently large. The second assumption is more debatable since, in general, mean velocity and mean orientation of the bacteria could decouple (e.g., if long-range hydrodynamic interactions are important). Our SPR simulations on the other hand suggest that, for very high filling fractions, orientation and velocity are strongly correlated. We therefore expect that the second assumption is reasonable for dense suspensions but becomes invalid at lower concentrations when bacteria assemble into inhomogeneous swarm-like structures [9]. In this flocking regime, see region (S) in Fig. 1A of the Main Text, more complex theories that take into account a locally varying bacterial concentration and distinguish between solvent velocity field, mean bacterial velocity field $\boldsymbol{v}(t, \boldsymbol{x})$ and mean bacterial orientation field provide a more adequate description of bacterial suspensions [14, 15, 16]. Another possible extension is the inclusion of additional higher-moment order-parameter fields like the $\boldsymbol{Q}$-tensor [17, 18], which encodes local fluctuations in the particle orientations. Due to the very large number of unknown coefficients, however, it seems very difficult if not impossible to constrain such more sophisticated models with the presently available experimental data. Here, we assume that the experimentally observed behavior can be reproduced from a suitably designed theory that only utilizes the flow field $\boldsymbol{v}$ which can be measured experimentally by PIV or tracking methods.

Field Equations. The incompressibility assumption is implemented by demanding that the flow field $\boldsymbol{v}(t, \boldsymbol{x})$ is divergence-free,

$$\nabla \cdot \boldsymbol{v} = \partial_i v_i = 0, \qquad i = 1, \ldots, d, \qquad [16]$$

where d is the number of space dimensions (throughout, we assume a sum over equal lower indices). We further postulate that the dynamics of $\boldsymbol{v}$ is governed by a generalized d-dimensional Navier-Stokes equation of the form

$$(\partial_t + \boldsymbol{v} \cdot \nabla)\boldsymbol{v} = -\nabla p - (\alpha + \beta |\boldsymbol{v}|^2)\boldsymbol{v} + \nabla \cdot \boldsymbol{E}, \qquad [17]$$

where the pressure p is the Lagrange multiplier for the incompressibility condition, α and β are parameters, and the rate-of-strain tensor $\boldsymbol{E}$ depends on $\boldsymbol{v}$ as specified below.

The second contribution on the rhs. of Eq. [17] is a typical local driving term as known from the Toner-Tu model [11, 12]. This term effectively corresponds to a quartic Landau-potential for the velocity order-parameter field $\boldsymbol{v}$. Stability requires that $\beta \geq 0$, while α is allowed to take positive or negative values. In the absence of other driving mechanisms, the Toner-Tu term drives the fluid to an isotropic

equilibrium state with $\boldsymbol{v} = 0$ if $\alpha > 0$, whereas for $\alpha < 0$ and $\beta > 0$ the velocity potential becomes 'bistable', leading to global polar ordering with characteristic speed

$$v_0 = \sqrt{|\alpha|/\beta}. \qquad [18]$$

To close the model equations, we still need to specify $\boldsymbol{E}$ in terms of $\boldsymbol{v}$ and its derivatives. Using guidance from the theory of active nematics [15], we postulate the components of the symmetric and trace-free rate-of-strain tensor $\boldsymbol{E}$ to have the form

$$E_{ij} = \Gamma_0(\partial_i v_j + \partial_j v_i) - \Gamma_2 \triangle (\partial_i v_j + \partial_j v_i) + S\, q_{ij}, \qquad [19]$$

where $\triangle = \nabla^2$ is the d-dimensional Laplacian, and

$$q_{ij} = v_i v_j - \frac{\delta_{ij}}{d}|\boldsymbol{v}|^2 \qquad [20]$$

is a mean-field approximation to the $\boldsymbol{Q}$-tensor (recalling our assumption that the direction of the velocity field coincides with mean local swimmer orientation), with the Kronecker-symbol δ_{ij} denoting elements of the unit matrix $\boldsymbol{I}$. For $\Gamma_0 > 0$ and $S = 0 = \Gamma_2$, Eq. [19] reduces to the usual rate-of-strain tensor of a conventional fluid with viscosity Γ_0. However, to obtain a minimal model of self-sustained turbulence in active suspensions, we shall allow for negative values $\Gamma_0 < 0$ while demanding in this case that $\Gamma_2 > 0$ to ensure stability of the theory (see detailed stability analysis below). The additional S-term in Eq. [19] presents an active stress contribution (in mean-field approximation) as known from theories of active nematics [15]. General hydrodynamic considerations [16] suggest that $S > 0$ for puller-type swimmers (e.g., algae), whereas $S < 0$ for pushers such as *B. subtilis*. Intuitively, one may regard the two Γ-terms in Eq. [19] as arising from a systematic (linear in $\boldsymbol{v}$) expansion of the stress-tensor, with the higher-order derivatives (Γ_2-term) accounting for longer-range multi-particle interactions.

Inserting Eq. [19] into Eq. [17], and defining

$$\lambda_0 = 1 - S, \qquad \lambda_1 = -S/d, \qquad [21]$$

we obtain

$$\begin{aligned}(\partial_t + \lambda_0 \boldsymbol{v}\cdot\nabla)\boldsymbol{v} &= -\nabla p + \lambda_1 \nabla \boldsymbol{v}^2 - (\alpha + \beta|\boldsymbol{v}|^2)\boldsymbol{v} + \\ &\quad \Gamma_0 \triangle \boldsymbol{v} - \Gamma_2 \triangle^2 \boldsymbol{v}. \qquad [22]\end{aligned}$$

As we shall see below, the two Γ-terms in Eq. [22], which are reminiscent of the higher-order derivatives in the Swift-Hohenberg theory [13], are essential for the formation of quasi-chaotic flow patterns in this model. These linear terms provide a simple (if not the simplest) generic description of turbulent instabilities in dense bacterial suspensions – and the resulting theory agrees remarkably with well both our experiments and particle simulations. More generally, we expect Eq. [22] to provide a satisfactory phenomenological description whenever interaction terms in more complex field theories, that lead to instabilities in the $\boldsymbol{v}$-field, can be effectively approximated by a fourth-order Taylor expansion in Fourier space, which is likely to be the case for a wide range of active systems. Phrased differently, the last two terms in Eq. [22] may be regarded as the Fourier-space analogue of the Toner-Tu driving terms, which correspond to a series expansion in terms of the order parameter.

Before presenting a linear stability analysis for the 'minimal' continuum model defined by Eqs. [16] and [22], let us still note that it is straightforward to construct extensions of the theory, e.g., by including density fluctuations or coupling to concentration fields.

2D Stability Analysis. We perform a stability analysis for the 2D case relevant to our particle simulations and quasi-2D experiments, assuming that $\Gamma_0 < 0$ and $\beta > 0$, $\Gamma_2 > 0$.

For arbitrary values of α, Eqs. [16] and [22] have a fixed point that corresponds to a disordered isotropic state

$$\mathcal{S}_i : (\boldsymbol{v}, p) = (\boldsymbol{0}, p_0), \qquad [23]$$

where p_0 is a pressure constant. For $\alpha < 0$, an additional class of fixed points arises, corresponding to a manifold of globally ordered polar states

$$\mathcal{S}_p : (\boldsymbol{v}, p) = (\boldsymbol{v}_0, p_0), \qquad [24]$$

where $\boldsymbol{v}_0$ is constant vector with arbitrary orientation and fixed swimming speed $|\boldsymbol{v}_0| = \sqrt{|\alpha|/\beta} =: v_0$.

(i) Stability of the disordered isotropic state $\mathcal{S}_i$. Linearizing Eqs. [16] and [22] for small velocity and pressure perturbations around the isotropic state, $\boldsymbol{v} = \boldsymbol{\varepsilon}$ and $p = p_0 + \eta$ with $|\eta| \ll |p_0|$, we have to leading order

$$\begin{aligned}0 &= \nabla\cdot\boldsymbol{\varepsilon}, \qquad [25]\\ \partial_t \boldsymbol{\varepsilon} &= -\nabla\eta - \alpha\boldsymbol{\varepsilon} + \Gamma_0\triangle\boldsymbol{\varepsilon} - \Gamma_2\triangle^2\boldsymbol{\varepsilon}. \qquad [26]\end{aligned}$$

Considering perturbations of the form

$$(\eta, \boldsymbol{\varepsilon}) = (\hat{\eta}, \hat{\boldsymbol{\varepsilon}}) e^{i\boldsymbol{k}\cdot\boldsymbol{x} + \sigma t} \qquad [27]$$

and defining $k = |\boldsymbol{k}|$, we find

$$\begin{aligned}0 &= \boldsymbol{k}\cdot\hat{\boldsymbol{\varepsilon}} \qquad [28]\\ \sigma\hat{\boldsymbol{\varepsilon}} &= -i\hat{\eta}\boldsymbol{k} - (\alpha + \Gamma_0 k^2 + \Gamma_2 k^4)\hat{\boldsymbol{\varepsilon}}. \qquad [29]\end{aligned}$$

Multiplying the second equation by $\boldsymbol{k}$ and using the incompressibility condition implies that $\hat{\eta} = 0$ and, therefore,

$$\sigma(\boldsymbol{k}) = -(\alpha + \Gamma_0 k^2 + \Gamma_2 k^4). \qquad [30]$$

Assuming $\Gamma_0 < 0$ and $\Gamma_2 > 0$, we find an unstable band of modes with $\sigma(\boldsymbol{k}) > 0$ for $k_-^2 < k^2 < k_+^2$, where

$$k_\pm^2 = \frac{|\Gamma_0|}{\Gamma_2}\left(\frac{1}{2} \pm \sqrt{\frac{1}{4} - \frac{\alpha\Gamma_2}{|\Gamma_0|^2}}\right) \qquad [31]$$

provided that

$$4\alpha < |\Gamma_0|^2/\Gamma_2. \qquad [32]$$

Note that for $\alpha < 0$ the isotropic state is generally unstable with respect to long-wave length (small-k) perturbations.

(ii) Stability of the ordered polar state $\mathcal{S}_p$. We next perform a similar analysis for the polar state $(\boldsymbol{v}_0, p_0)$, which exists for $\alpha < 0$. This state corresponds to all particles swimming in the same direction. In this case, when considering small deviations

$$\boldsymbol{v} = \boldsymbol{v}_0 + \boldsymbol{\varepsilon}, \qquad p = p_0 + \eta, \qquad [33]$$

it is useful to distinguish perturbations perpendicular and parallel to $\boldsymbol{v}_0$, by writing $\boldsymbol{\varepsilon} = \boldsymbol{\varepsilon}_{||} + \boldsymbol{\varepsilon}_\perp$ where $\boldsymbol{v}_0\cdot\boldsymbol{\varepsilon}_\perp = 0$ and $\boldsymbol{v}_0\cdot\boldsymbol{\varepsilon}_{||} = v_0\varepsilon_{||}$. Without loss of generality, we may choose $\boldsymbol{v}_0$ to point along the x-axis, $\boldsymbol{v}_0 = v_0\boldsymbol{e}_x$. Adopting this convention, we have $\boldsymbol{\varepsilon}_{||} = (\varepsilon_{||}, 0)$ and $\boldsymbol{\varepsilon}_\perp = (0, \varepsilon_\perp)$, and to leading order

$$|\boldsymbol{v}|^2 \simeq v_0^2 + 2v_0\varepsilon_{||}. \qquad [34]$$

Again considering exponential perturbations of the form

$$(\eta, \varepsilon_{||}, \varepsilon_\perp) = (\hat{\eta}, \hat{\varepsilon}_{||}, \hat{\varepsilon}_\perp)\, e^{i\boldsymbol{k}\cdot\boldsymbol{x} + \sigma t}, \qquad [35]$$

we find in linear approximation

$$\begin{aligned}0 &= \boldsymbol{k}\cdot\hat{\boldsymbol{\varepsilon}}, \qquad [36]\\ \sigma\,\hat{\boldsymbol{\varepsilon}} &= -i(\hat{\eta} - 2v_0\lambda_1\hat{\varepsilon}_{||})\boldsymbol{k} + \boldsymbol{A}\hat{\boldsymbol{\varepsilon}}, \qquad [37]\end{aligned}$$

where

$$\boldsymbol{A} = \begin{pmatrix} 2\alpha & 0 \\ 0 & 0 \end{pmatrix} - (\Gamma_0 k^2 + \Gamma_2 k^4 + i\lambda_0 k_x v_0)\boldsymbol{I} \qquad [38]$$

with $\boldsymbol{I}$ denoting the identity matrix. Multiplying Eq. [37] with $i\boldsymbol{k}$, and using the incompressibility condition [36], gives

$$\hat{\eta} = 2v_0\lambda_1\varepsilon_{||} - i\frac{\boldsymbol{k}\cdot(\boldsymbol{A}\hat{\boldsymbol{\varepsilon}})}{k^2}. \qquad [39]$$

Inserting this into Eq. [37] and defining $\boldsymbol{A}_\perp = \boldsymbol{\Pi}(\boldsymbol{k})\boldsymbol{A}$, where

$$\Pi_{ij}(\boldsymbol{k}) := \delta_{ij} - \frac{k_i k_j}{k^2} \qquad [40]$$

is the orthogonal projector of $\boldsymbol{k}$, we obtain

$$\sigma\,\hat{\boldsymbol{\varepsilon}} = \boldsymbol{A}_\perp\,\hat{\boldsymbol{\varepsilon}}. \qquad [41]$$

The eigenvalue spetrum of the matrix $\boldsymbol{A}_\perp$ is given by

$$\sigma(\boldsymbol{k}) \in \left\{0, -\left(\Gamma_0 k^2 + \Gamma_2 k^4 - 2\alpha\frac{k_x^2}{k^2}\right) - i\lambda_0 v_0 k_x\right\}. \qquad [42]$$

The zero eigenvalues correspond to the Goldstone modes. The non-zero eigenvalues have eigenvectors $(-k_y, k_x)$, implying that, for $\Gamma_0 < 0$, there will be a range of exponentially growing k-modes in the direction perpendicular to $\boldsymbol{k}$.

We may thus summarize: Eqs. [30] and [42] show that, for $\alpha < 0$ and $\Gamma_0 < 0$, the two fixed points become simultaneously unstable, indicating the existence of a quasi-stationary spatially inhomogeneous dynamic attractor. By contrast, for $\Gamma_0 > 0$ the polar state becomes stable, as evident from Eq. [42]. More generally, the above analysis suggests that the combination of the two Γ-terms is arguably the simplest linear way of constructing a $\boldsymbol{v}$-only theory with non-trivial stationary dynamics within the class of 'standard' partial differential equations. We note that, in principle, it would also be possible to generate similar instabilities by combining odd or fractional powers of k in Eqs. [30] and [42]; this would be somewhat similar to replacing the quartic Landau potential by a more general function of $|\boldsymbol{v}|$. However, when considering eigenvalue spectra based on odd or non-integer powers of k, the underlying dynamical equations in position space would correspond to fractional partial differential equations. One may speculate that such fractional models could potentially be useful for modeling active suspensions with long-range or other types of more complex interactions. The comparison with our quasi-2D experiments, however, illustrates that Eqs. [16] and [22] provide a useful continuum description of dense bacterial suspensions.

Guidance for Numerical Parameters Estimation. The minimal model from in Eqs. [16] and [22] features a relatively small number of parameters, which can be constrained by comparison with experiments. For $\alpha < 0$ the polar velocity $v_0 = \sqrt{|\alpha|/\beta}$ should be approximately equal to the swimming speed of a bacterium in suspension. Γ_0 and Γ_2 define characteristic length and velocity scales

$$\Lambda = \sqrt{\Gamma_2/|\Gamma_0|}, \qquad V_\Gamma = \sqrt{|\Gamma_0|^3/\Gamma_2}, \qquad [43]$$

that can be roughly estimated from the characteristic vortex size and swimming velocity of the bacteria, thereby yielding approximate values for Γ_0 and Γ_2 that can be used as starting points for systematic parameter scans in numerical simulations.

Furthermore, the parameter α defines a characteristic damping (acceleration) time-scale

$$\tau_\alpha = 1/|\alpha| \qquad [44]$$

in the isotropic case $\alpha > 0$ (polar case $\alpha < 0$). To obtain turbulent states, this time scale τ_α must be much larger than the time scale for the growth of instabilities

$$\tau_\Gamma = \Gamma_2/|\Gamma_0|^2, \qquad [45]$$

which roughly correspond to the maximum of the real part of $\sigma(\boldsymbol{k})$ in Eqs. [30] and [42]. Hence, the criterion for active mesoscale turbulence can be formulated as

$$R := \frac{\tau_\alpha}{\tau_\Gamma} = \frac{|\Gamma_0|^2}{\Gamma_2|\alpha|} \gg 1, \qquad [46]$$

which is consistent with Eq. [32]. In this regime, simulation time steps must be chosen much smaller than τ_Γ.

As stated above, for pusher-type swimmers like *E. coli* or *B. subtilis*, the dimensionless nematic order parameter S should be negative [16]. Intuitively, negative values of S increase both the convective non-linearity (via λ_0) and the local pressure (via λ_1). In our simulations, we found that moderate values $|S| \sim (1 \div 3)$ typically produce good agreement with our experimental data.

Finally, the parameter β in the fourth-order term of the Landau potential determines the damping of large velocities. To reproduce the Gaussian velocity statistics observed in experiments, β must be chosen sufficiently small in simulations. It should be stressed that the quartic velocity potentials, which essentially arises from a small-$|\boldsymbol{v}|$ expansion, becomes inaccurate for large velocities. Therefore, one cannot expect that hydrodynamic models that are based on such Landau-type approximations correctly capture the tails of the velocity statistics in bacterial suspensions. Nevertheless, as our study shows, these models are able to describe the main phenomenological aspects of active meso-scale turbulence.

Simulation Parameters. In our 2D simulations of Eqs. [16] and [22], we use periodic boundary conditions and adopt characteristic units such that the length L of the quadratic simulation box is given by $L = \pi$ and the velocity scale by $V_\Gamma = \sqrt{|\Gamma_0|^3/\Gamma_2} = 1$. The remaining parameters are tuned such that the flow characteristics (number of vortices, spectral properties, etc.) in the simulated volume match the experimental quasi-2D data for *B. subtilis* as closely as possible. To compare simulation results with experiments, we assume that $v_0 \sim 35\mu$m/s in physical units while fixing the conversion factor for the box length L such that the typical vortex size in the experiments agrees with that in the simulations. For example, for the parameters used in Figs. 2-4 of the Main Text (which are listed in the Table below), the length of the simulation box corresponds to $L \sim 150\,\mu$m, which is comparable to the experimental field of view and implies that simulation time is measured in units of $T_0 = (L/\pi)/V_\Gamma \sim 1.9$ s. Hence, one minute in real time equals a simulation period $T \sim 30$ in characteristic units. After systematically scanning a wide range of parameters, we found that the following values yield good agreement with the quasi-2D *B. subtilis* experiments:

parameter	rescaled value in simulations	value	units
box size L	π	150	μm
V_Γ	1	25	μm/s
α	-1	-0.5	1/s
β	0.5	4×10^{-4}	s/μm^2
Γ_0	-0.045	-53	μm^2/s
Γ_2	$\lvert\Gamma_0\rvert^3$	245	μm^4/s
S	-2.5	-2.5	1

With these parameters, the continuum model correctly reproduces the main equal-time statistical quantifiers (see Fig. 3 and 4 in the Main Text) and also the approximately exponential decay of the two-time autocorrelations $\langle \boldsymbol{v}(t,\boldsymbol{r})\boldsymbol{v}(t',\boldsymbol{r})\rangle$ of the quasi-2D experimental data (see Fig. S9 below). For both experiments and simulations, the typical correlation time is of the order of 0.5 s which corresponds approximately to the typical vortex size (a few ℓ) divided by the polar speed v_0.

Numerical Methods. To simulate the 2D continuum model with periodic boundary conditions, we used a pseudo-spectral algorithm as commonly employed in computational fluid dynamics [19]. The model equations were transformed into Fourier space and the resulting set of ordinary differential equations were solved numerically by an integrating factor method that solves the linear terms exactly [20]. The results were cross-checked with an implicit-explicit Euler integration [21]. In both schemes, nonlinear terms were treated carefully by implementing the 2/3-rule to suppress aliasing errors [22]. This means that, for quadratic nonlinearities, wave-vectors corresponding to wavelengths larger than 2/3 of the box size are set to zero and, similarly, for higher-order terms. Therefore, the effective spatial grid-size is smaller than the one used in the fluid solver. In our simulations, we tested different effective grid-sizes, ranging from 64×64 to 256×256 lattice points. Typical time steps used were of the order $\Delta t = 10^{-4}$ in dimensionless units as introduced above (specifically, $\Delta t = 2\times10^{-4}$ for the figures in the Main Text). To ensure that the flow vector fields remain divergence-free, the hydrodynamic pressure p is calculated using a pressure correction routine. Our fluid solver was written in Matlab and stability of the code was verified for a wide range of parameters.

Simulations were initiated with isotropic randomly chosen flow field configurations $\boldsymbol{v}(0,\boldsymbol{x})$ and were allowed to relax for 10^4 time steps, before data for the velocity fields were stored. Thereafter, snapshots were generated with a separation of 1000 time steps between successive outputs. In our statistical analysis we typically used data from $\sim$ 900 snapshots.

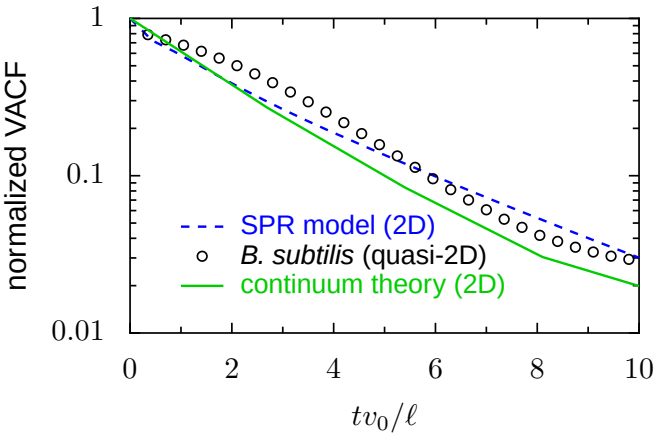

Fig. S9. The two-time velocity autocorrelation functions (VACFs) $\langle \boldsymbol{v}(t,\boldsymbol{r})\boldsymbol{v}(t',\boldsymbol{r})\rangle$, normalized by $\langle \boldsymbol{v}^2\rangle$, decay approximately exponentially for both experimental and model data. To rescale the time-axis, we used for the SPR model the rod length ℓ and $v_0 = V$, where V is free rod speed as defined by Eq. **[12]**, whereas for the experiments and the continuum theory we used the bacterial length $\ell = 4.8\,\mu$m and $v_0 = \sqrt{|\alpha|/\beta} = 35\,\mu$m/s as obtained from the parameters given in the Table above. The good quantitative agreement shows that the 2D continuum theory can reproduce not only the main characteristics of equal-time statistics (see Fig. 3 and 4 in the Main Text) but also the most relevant dynamical features of the quasi-2D *B. subtilis* experiments.

Supplementary Movie Information

Supplementary Movies S1-S6 represent results of the SPR simulations. Each of those movies shows the dynamics in a subsection of the total simulation volume (with comparable mean particle number) over the last 20% of the total simulations time interval. Simulation parameters are the same as in Fig. S2. Movies S7-S10 show representative movie data from quasi-2D and 3D experiments as used for the statistical analysis in the Main Text. Raw data and higher-resolution movies can be downloaded from http://damtp.cam.ac.uk/user/gold/datarequests.html

1. Kirchhoff, T, Löwen, H, & Klein, R. (1996) Dynamical correlations in suspensions of charged rodlike macromolecules. Phys. Rev. E 53, 5011–5022.
2. Drescher, K, Dunkel, J, Cisneros, L. H, Ganguly, S, & Goldstein, R. E. (2011) Fluid dynamics and noise in bacterial cell-cell and cell-surface scattering. Proc. Natl. Acad. Sci. USA 108, 10940–10945.
3. Tirado, M. M, de la Torre, J. G, & Martinez, C. L. (1984) Comparison of theories for the translational and rotational diffusion coefficients of rod-like macromolecules. Application to short DNA fragments. J. Chem. Phys. 81, 2047–2052.
4. Cisneros, L. H, Cortez, R, Dombrowski, C, Goldstein, R. E, & Kessler, J. O. (2007) Fluid dynamics of self-propelled micro-organisms, from individuals to concentrated populations. Experiments in Fluids 43, 737–753.
5. Cisneros, L. H, Kessler, J. O, Ganguly, S, & Goldstein, R. E. (2011) Dynamics of swimming bacteria: Transition to directional order at high concentration. Phys. Rev. E 83, 061907.
6. Zhang, H. P, Be'er, A, Smith, R. S, Florin, E, & Swinney, H. L. (2009) Swarming dynamics in bacterial colonies. EPL 87, 48011.
7. Sokolov, A, Aranson, I. S, Kessler, J. O, & Goldstein, R. E. (2007) Concentration dependence of the collective dynamics of swimming bacteria. Phys. Rev. Lett. 98, 158102.
8. Chen, X, Dong, X, Be'er, A, Swinney, H. L, & Zhang, H. P. (2012) Scale-invariant correlations in dynamic bacterial clusters. Phys. Rev. Lett. 108, 148101.
9. Zhang, H. P, Be'er, A, Florin, E.-L, & Swinney, H. L. (2010) Collective motion and density fluctuations in bacterial colonies. Proc. Natl. Acad. Sci. USA 107, 13626–13630.
10. Volfson, D, Cookson, S, Hasty, J, & Tsimring, L. S. (2008) Biomechanical ordering of dense cell populations. Proc. Natl. Acad. Sci. USA 150, 15346–15351.
11. Toner, J & Tu, Y. (1995) Long-range order in a two-dimensional dynamical xy model: How birds fly together. Phys. Rev. Lett. 75, 4326–4329.
12. Toner, J & Tu, Y. (1998) Flocks, herds, and schools: A quantitative theory of flocking. Phys. Rev. E 58, 4828–4858.
13. Swift, J & Hohenberg, P. C. (1977) Hydrodynamic fluctuations at the convective instability. Phys. Rev. A 15, 319–328.
14. Wolgemuth, C. W. (2008) Collective swimming and the dynamics of bacterial turbulence. Biophys. J. 95, 1564–1574.
15. Ramaswamy, S. (2002) Hydrodynamic fluctuations and instabilities in ordered suspensions of self-propelled particles. Phys. Rev. Lett. 89, 058101.
16. Pedley, T. J. (2010) Collective behaviour of swimming micro-organisms. Experimental Mechanics 50, 1293–1301.
17. de Gennes, P. G & Prost, J. (1995) The Physics of Liquid Crystals. (Oxford University Press, Oxford) Vol. 2.
18. Baskaran, A & Marchetti, M. C. (2008) Hydrodynamics of self-propelled hard rods. Phys. Rev. E 77, 011920.
19. Gottlieb, D & Orszag, S. A. (1977) Numerical analysis of spectral methods: Theory and applications. (SIAM, Philadelphia).
20. Pedrosa, J, Hoyuelos, M, & Martel, C. (2008) Numerical validation of the complex swift-hohenberg equation for lasers. Eur. Phys. J. B 66, 525–530.
21. Ascher, U. M, Ruuth, S. J, & Wetton, B. T. R. (1996) Implicit-explicit methods for time-dependent partial differential equations. SIAM J. Numer. Anal. 32, 797–823.
22. Canuto, C, Hussaini, M. Y, Quarteroni, A, & Zang, T. A. (2006) Spectral methods: fundamentals in single domains. (Springer, Berlin).

Supporting Information

Wensink et al. 10.1073/pnas.1202032109

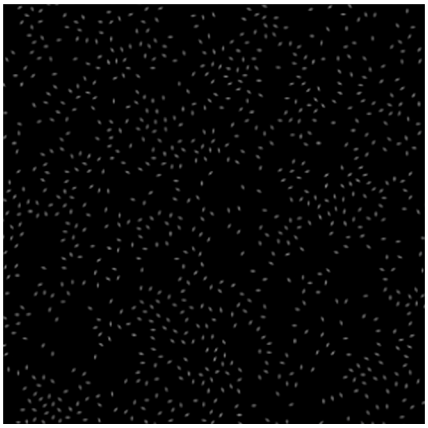

Movie S1. Dilute phase of the SPR model. Same parameters as in *SI Appendix* Fig. S2*A*.

Movie S1 (MOV)

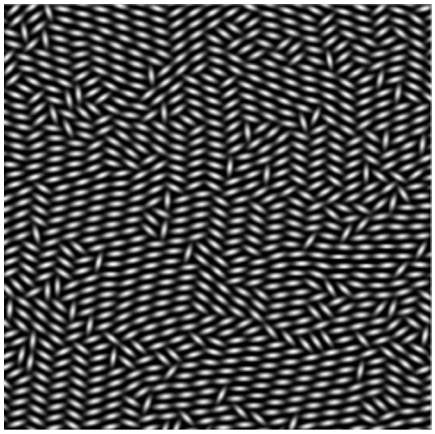

Movie S2. Jamming phase of the SPR model. Same parameters as in *SI Appendix* Fig. S2*B*.

Movie S2 (MOV)

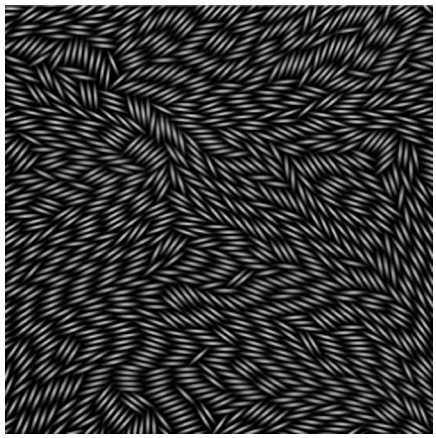

Movie S3. Bionematic phase of the SPR model. Same parameters as in *SI Appendix* Fig. S2*C*.

Movie S3 (MOV)

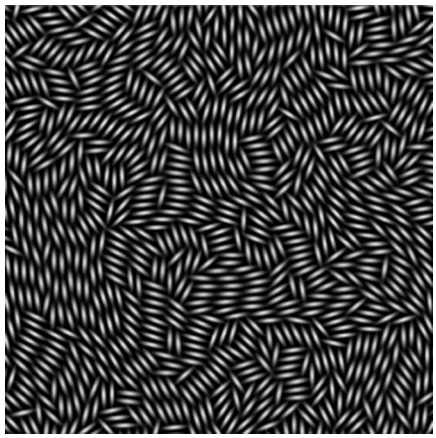

Movie S4. Turbulent phase of the SPR model. Same parameters as in *SI Appendix* Fig. S2*D*.

Movie S4 (MOV)

Movie S5. Swarming phase of the SPR model. Same parameters as in *SI Appendix* Fig. S2*E*.

Movie S5 (MOV)

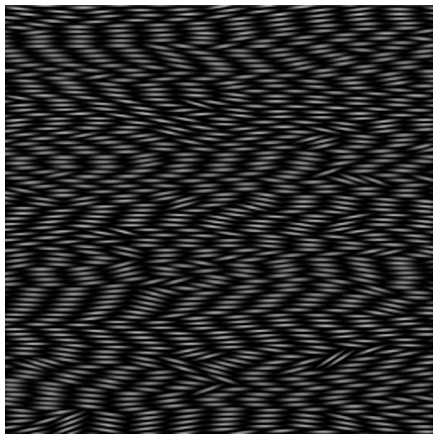

Movie S6. Laning phase of the SPR model. Same parameters as in *SI Appendix* Fig. S2*F*.

Movie S6 (MOV)

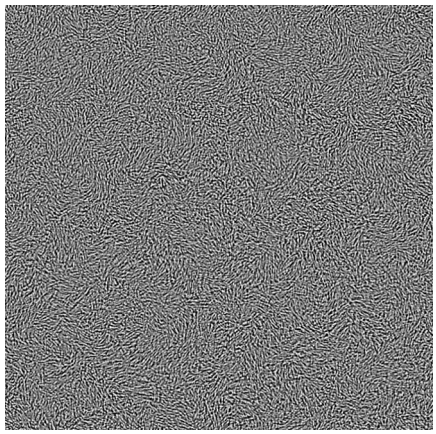

Movie S7. Turbulent phase in a quasi-2D homogeneous *B. subtilis* suspension (channel thickness approximately 5 μm).

Movie S7 (MOV)

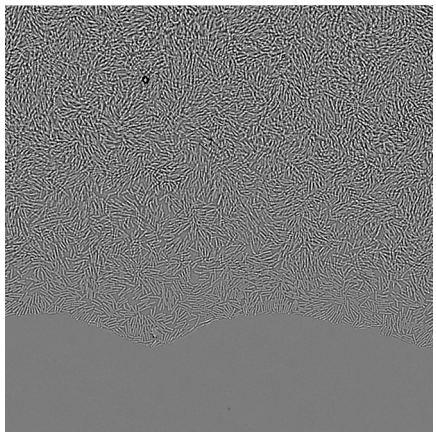

Movie S8. Diluted phase in a quasi-2D *B. subtilis* suspension (channel thickness approximately 5 μm) near a liquid–air boundary. Bacterial aspect ratios (see *SI Appendix*, Fig. S7) were determined from the diluted 2D layer near the boundary.

Movie S8 (MOV)

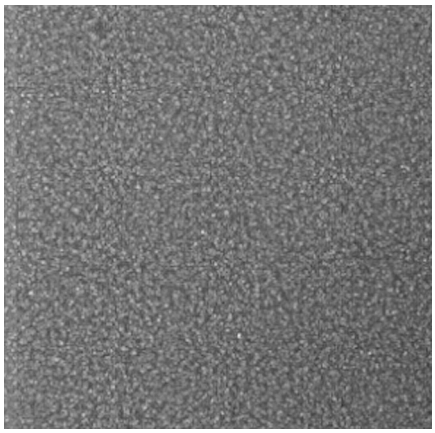

Movie S9. Turbulent phase in a 3D *B. subtilis* suspension (channel thickness approximately 80 μm), imaged close (approximately 10 μm) to the lower chamber boundary.

Movie S9 (MOV)

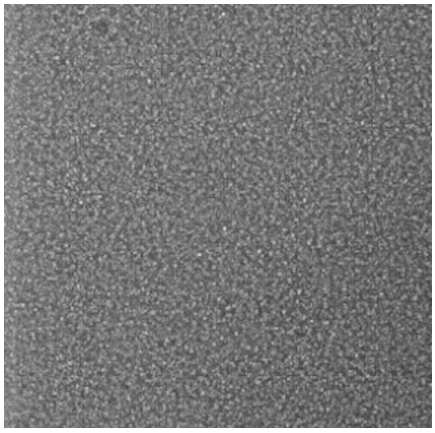

Movie S10. Turbulent phase in a 3D *B. subtilis* suspension (channel thickness approximately 80 μm), imaged in the bulk fluid approximately 40 μm from the lower channel wall. Results for 3D data shown in the main text correspond to these bulk measurements.

Movie S10 (MOV)